SWASH: an operational public domain code for simulating wave fields and rapidly varied flows in coastal waters

Marcel Zijlema [1], Guus Stelling and Pieter Smit

Environmental Fluid Mechanics Section, Faculty of Civil Engineering and Geosciences, Delft University of Technology, P.O. Box 5048, 2600 GA Delft, The Netherlands

Abstract

A computational procedure has been developed for simulating non-hydrostatic, free-surface, rotational flows in one and two horizontal dimensions. Its implementation in the publicly available SWASH (an acronym of Simulating WAves till SHore) is intended to be used for predicting transformation of surface waves and rapidly varied shallow water flows in coastal waters. This open source code (http://swash.sourceforge.net) has been developed based on the work of Stelling and Zijlema (2003), Stelling and Duinmeijer (2003) and Zijlema and Stelling (2005, 2008). The governing equations are the nonlinear shallow water equations including non-hydrostatic pressure and provide a general basis for describing complex changes to rapidly varied flows typically found in coastal flooding resulting from e.g. dike breaks and tsunamis, and wave transformation in both surf and swash zones due to nonlinear wave-wave interactions, interaction of waves with currents, and wave breaking as well as runup at the shoreline. The present paper provides a complete description of the numerical algorithms currently used in the code. The code is benchmarked using some analytical

problems. Moreover, the numerical results are validated with various cases of laboratory data with the principal aim to convey the capabilities of the SWASH code. In particular, emphasis is put on an analysis of model performance and associated physical implications. Serial and parallel performance scalings are also presented.

Key words: Non-hydrostatic modeling, Surf zone, Wave propagation, Wave breaking, Rapidly varied flows, Shoreline tracking

1 Introduction

Rapid advances in computer hardware and numerical methods in recent years have made it possible to solve the Reynolds-averaged Navier-Stokes equations for water waves, in which the vertical structure is calculated simultaneously with the horizontal variations. Well-known methods for the treatment of the free surface are described in the literature, e.g. the Volume-of-Fluid (VOF) and Smoothed Particle Hydrodynamics (SPH) methods (Hirt and Nicols, 1981; Dalrymple and Rogers, 2006). However, in the context of feasible and efficient simulations of large-scale wave evolution and shallow water flows in ocean and coastal seas, an approach is adopted in which the free-surface motion is tracked using a single-valued function of the horizontal plane. The most commonly applied model using this technique is often non-hydrostatic of nature. Non-hydrostatic models consist of the nonlinear shallow water (NLSW) equations with the addition of a vertical momentum equation and non-hydrostatic pressure in horizontal momentum equations. These models require much fewer

[1] Tel.: +31 15 278 3255; fax: +31 15 278 4842.

E-mail address: m.zijlema@tudelft.nl

grid cells in the vertical direction than the VOF and SPH methods. In addition, the NLSW equations with appropriate conservation properties are able to deal accurately with large gradients or discontinuities in the flow, such as hydraulic jumps and bores, near steep bottom gradients. Examples are dike breach flooding and tsunami inundation. Moreover, the combined effects of wave-wave and wave-current interaction in shallow water are automatically included in a non-hydrostatic wave-flow model and do not need any additional modelling. It is this recognition which invoked the efforts to which the present paper relates.

Non-hydrostatic modelling of water wave dynamics is not new; more than 10 years have elapsed since the pioneering contributions of Casulli and Stelling (1998) and Stansby and Zhou (1998). Since then, several papers on this topic in the context of coastal modelling activities have been published; see Yamazaki et al. (2009), Young and Wu (2010) and Ai et al. (2010), to mention a few recent papers. The objectives pursued in these studies have varied considerably. Frequently, however, the general emphasis has been on developing an accurate and efficient computational procedure capable of simulating relatively short wave propagation, where both frequency dispersion and nonlinear effects play an important role. This issue is sufficiently fundamental to be common to the majority of idealised wave conditions in a laboratory environment, and it is on this type of conditions that studies tended to concentrate, if only because of the availability of experimental data suitable for validation. For example, accurate measurements for wave transformation over submerged bars and shoals have been obtained by Berkhoff et al. (1982), Beji and Battjes (1993), Ohyama et al. (1995) and Chawla (1995). However, it is more evolved to assess such numerical models at an operational level with laboratory or

perhaps field measurements under realistic nearshore conditions. So far, no advances have been made in applying non-hydrostatic models to such realistic laboratory experiments or field campaigns in the surf zone.

Over the past 10 years, strong efforts have been made at Delft University to advance the state of wave modelling and flooding simulations for coastal engineering applications. These efforts have focused on developing and validating the well-known spectral wave model SWAN (Booij et al., 1999) and the newly developed non-hydrostatic model SWASH. The purpose of the present work is to report on the experiences that have been gathered in the development of SWASH for surface waves and rapidly varied flows at every Froude number in coastal areas. Parts of this work have progressed initially within a simple one-dimensional flume involving non-breaking, regular, short waves, hydraulic jumps and dam break over dry and wet beds. Major objectives pursued at that stage included an implementation of a compact scheme for vertical pressure gradients resolving frequency dispersion in conjunction with a careful assessment of linear wave properties, such as dispersion and shoaling, by reference to data emerging from experimental studies (Stelling and Zijlema, 2003), an efficient and stable implementation of a Poisson solver for the non-hydrostatic pressure (Zijlema and Stelling, 2005), and an efficient implementation of an advection scheme on staggered grids enabling to conserve momentum locally or, by choice, preserve constant energy head along a streamline (Stelling and Duinmeijer, 2003). More recently, there have been efforts to branch into more challenging wave features within the surf and swash zones, like irregular breaking waves and their runup over foreshores, by applying the aforementioned momentum-conservative scheme and a simple wet-dry algorithm, respectively (Zijlema and Stelling, 2008), and into more complicated geometries, e.g. coast-

lines and around islands, by means of algorithms using unstructured meshes (Kramer and Stelling, 2008; Cui et al., 2010).

The above issues are among many addressed in the course of evolving the SWASH code for operational use, which combines the following main elements and characteristics:

- It is based on an explicit, second order finite difference method for staggered grids whereby mass and momentum are strictly conserved at discrete level. As a consequence, this simple and efficient scheme is able to track the actual location of incipient wave breaking. Also, momentum conservation enables the broken waves to propagate with a correct gradual change of form and to resemble steady bores in a final stage. Yet, this approach is appropriate for hydraulic jumps, dam-break problems and flooding situations as well.
- With respect to time integration of the continuity and momentum equations, the second order leapfrog scheme (Hansen, 1956) is adopted, as it does not alter the wave amplitude while its numerical dispersion is favourable.
- In order to resolve the frequency dispersion up to an acceptable level of accuracy, a compact difference scheme for the approximation of vertical gradient of the non-hydrostatic pressure is applied in conjunction with a vertical terrain-following grid, permitting more resolution near the free surface as well as near the bottom. This scheme receives good linear dispersion up to $kd \approx 7$ and $kd \approx 3$ with two equidistant layers at 1% error in phase velocity of standing and progressive waves, respectively (k and d are the wave number and still water depth, respectively). The model improves its frequency dispersion by simply increasing the number of vertical layers.
- The energy dissipation of the wavebreaker-generated turbulence is modelled with a Prandtl mixing length hypothesis.

- For a proper representation of the interface of water and land, a simple approach is adopted that tracks the moving shoreline by ensuring non-negative water depths and using the upwind water depths in the momentum flux approximations.

The model is essentially applicable in the coastal regions up to the shore. This has prompted the acronym SWASH for the associated code, standing for Simulating WAves till SHore. The basic philosophy of the SWASH code is to provide an efficient and robust model that allows a wide range of time and space scales of surface waves and shallow water flows in complex environments to be applied. As a result, SWASH allows for the entire modelling process to be carried out in any area of interest. SWASH is close in spirit to SWAN (Simulating WAves Nearshore) with respect to the pragmatism employed in the development of the code in the sense that comprises are sometimes necessary for reasons of efficiency and robustness. Furthermore, like SWAN, the software package of SWASH includes user-friendly pre- and post-processing and does not need any special libraries. In addition, SWASH is highly flexible, accessible and easily extendible concerning several functionalities of the model. As such, SWASH can be used operationally and the software can be used freely under the GNU GPL license (http://swash.sourceforge.net).

In this paper we present a comprehensive description of the SWASH code and its main results. Here, only those features are discussed that impinge on the above characteristics of SWASH and associated issues in related sections, occasionally referring to earlier publications to promote brevity. Applications drawn from the work of the Fluid Mechanics research group at Delft University convey an impression of the capabilities of SWASH.

2 Governing equations and boundary conditions

The most general coordinate framework that can be used in SWASH is curved orthogonal, and the governing equations may in principle be written in terms of these coordinates. However, such a form is unnecessarily complicated for the present purpose of outlining the principles adopted. Instead, the equations are introduced in terms of Cartesian notation. To simplify the statements without introducing a significant loss of generality, attention is focused on the depth-averaged flow in a two-dimensional horizontal physical domain. The extension to the three-dimensional framework is elaborated in Zijlema and Stelling (2005, 2008).

The depth-averaged, non-hydrostatic, free-surface flow can be described by the nonlinear shallow water equations that, in turn, can be derived from the incompressible Navier-Stokes equations that comprise the conservation of mass and momentum. These equations are given by

$$\frac{\partial \zeta}{\partial t} + \frac{\partial hu}{\partial x} + \frac{\partial hv}{\partial y} = 0 \tag{1}$$

$$\frac{\partial u}{\partial t} + u\frac{\partial u}{\partial x} + v\frac{\partial u}{\partial y} + g\frac{\partial \zeta}{\partial x} + \frac{1}{h}\int_{-d}^{\zeta} \frac{\partial q}{\partial x}\, dz + c_f \frac{u\sqrt{u^2+v^2}}{h} = \frac{1}{h}\left(\frac{\partial h\tau_{\mathrm{xx}}}{\partial x} + \frac{\partial h\tau_{\mathrm{xy}}}{\partial y}\right) \tag{2}$$

$$\frac{\partial v}{\partial t} + u\frac{\partial v}{\partial x} + v\frac{\partial v}{\partial y} + g\frac{\partial \zeta}{\partial y} + \frac{1}{h}\int_{-d}^{\zeta} \frac{\partial q}{\partial y}\, dz + c_f \frac{v\sqrt{u^2+v^2}}{h} = \frac{1}{h}\left(\frac{\partial h\tau_{\mathrm{yx}}}{\partial x} + \frac{\partial h\tau_{\mathrm{yy}}}{\partial y}\right) \tag{3}$$

where t is time, x and y are located at the still water level and the $z-$axis pointing upwards, $\zeta(x,y,t)$ is the surface elevation measured from the still water level, $d(x,y)$ is the still water depth, or downward measured bottom level, $h = \zeta + d$ is the water depth, or total depth, $u(x,y,t)$ and $v(x,y,t)$ are the depth-averaged flow velocities in $x-$ and $y-$directions, respectively,

$q(x, y, z, t)$ is the non-hydrostatic pressure (normalized by the density), g is gravitational acceleration, c_f is the dimensionless bottom friction coefficient, and τ_{xx}, τ_{xy}, τ_{yx} and τ_{yy} are the horizontal turbulent stress terms. Note that the momemtum equations are written in a non-conservative form. This will be discussed later. The integral of the non-hydrostatic pressure gradient over the water depth in Eq. (2) can be expressed as follows (Stelling and Zijlema, 2003):

$$\int_{-d}^{\zeta} \frac{\partial q}{\partial x}\, dz = \frac{1}{2}\, h \frac{\partial q_b}{\partial x} + \frac{1}{2}\, q_b \frac{\partial(\zeta - d)}{\partial x} \tag{4}$$

with q_b the non-hydrostatic pressure at the bottom. Similar expression can be found for the integral in Eq. (3).

Since the quantity q_b is included, some extra equations are needed. As demonstrated in Stelling and Zijlema (2003) the accuracy of the frequency dispersion for relative short waves can be significantly improved by applying the Keller-box method (Lam and Simpson, 1976):

$$\frac{q|_{z=\zeta} - q|_{z=-d}}{h} = -\frac{q_b}{h} = \frac{1}{2}\frac{\partial q}{\partial z}|_{z=\zeta} + \frac{1}{2}\frac{\partial q}{\partial z}|_{z=-d} \tag{5}$$

Note that the non-hydrostatic pressure at the free surface is zero. Next, we introduce the velocity in $z-$direction at the free surface, w_s, and at the bed level, w_b. The momentum equations for these vertical components are

$$\frac{\partial w_s}{\partial t} + \frac{\partial q}{\partial z}|_{z=\zeta} = 0\,, \quad \frac{\partial w_b}{\partial t} + \frac{\partial q}{\partial z}|_{z=-d} = 0 \tag{6}$$

where both the advective and diffusive terms have been neglected as they are generally small compared to the vertical acceleration which is assumed to be instantenously determined by the non-hydrostatic pressure gradient.

Combination of (6) and (5) gives

$$\frac{\partial w_{\mathrm{s}}}{\partial t} = \frac{2q_{\mathrm{b}}}{h} - \frac{\partial w_{\mathrm{b}}}{\partial t} \tag{7}$$

The vertical velocity at the bottom, w_{b}, can be found through the following kinematic condition:

$$w_{\mathrm{b}} = -u\frac{\partial d}{\partial x} - v\frac{\partial d}{\partial y} \tag{8}$$

Finally, conservation of local mass yields

$$\frac{\partial u}{\partial x} + \frac{\partial v}{\partial y} + \frac{w_{\mathrm{s}} - w_{\mathrm{b}}}{h} = 0 \tag{9}$$

When waves are travelling over a relatively long distance of order of several kilometres, the influence of bottom friction becomes more pronounced. Moreover, it may affect long waves close to the shoreline, e.g. infragravity waves, and nearshore circulations. Although there are many expressions for the bottom friction coefficient c_f, we employ the one based on Manning's roughness coefficient n, as follows,

$$c_f = \frac{n^2 g}{h^{1/3}} \tag{10}$$

since our experiences have indicated that this expression provides a better representation of wave dynamics in the surf zone to that returned by other well-known friction formulations such as the one in terms of the Chézy coefficient and the Colebrook-White equation.

The turbulent stresses are given by

$$\tau_{\mathrm{xx}} = 2\nu_{\mathrm{t}}\frac{\partial u}{\partial x}\,, \quad \tau_{\mathrm{xy}} = \tau_{\mathrm{yx}} = \nu_{\mathrm{t}}\left(\frac{\partial v}{\partial x} + \frac{\partial u}{\partial y}\right)\,, \quad \tau_{\mathrm{yy}} = 2\nu_{\mathrm{t}}\frac{\partial v}{\partial y} \tag{11}$$

with $\nu_t(x, y, t)$ the horizontal eddy viscosity due to wave breaking and sub-grid turbulence. In this paper, we restrict ourselves to the description of the breaking process. In this case a turbulence model needs to be employed to approximate the turbulent mixing and dissipation caused by breaking. Although dissipation is implicit in the bore representation, it is the viscosity that determine the scale at which dissipation takes place. As such, the large-scale turbulent motion in the surface roller can be effectively modelled through the eddy viscosity ν_t, whereby the turbulence is assumed to be in local equilibrium. For this reason, the Prandtl mixing length hypothesis is used and is given by

$$\nu_t = \ell_m^2 \sqrt{2\left(\frac{\partial u}{\partial x}\right)^2 + 2\left(\frac{\partial v}{\partial y}\right)^2 + \left(\frac{\partial v}{\partial x} + \frac{\partial u}{\partial y}\right)^2} \tag{12}$$

with ℓ_m the mixing length taken to be proportional to a typical wave height; either wave height for regular waves or significant wave height for irregular waves. It should be noted that this type of modelling should not only be regarded as modelling the lateral mixing but also as modelling the longitudinal momentum exchange occuring in the travelling turbulent bore.

To complete the system of equations, appropriate boundary conditions need to be imposed at the open boundaries of the computational grid domain. At the offshore boundary regular or irregular waves are introduced by specifying a local velocity distribution. To simulate entering waves without some reflections at this boundary, a weakly reflective condition allowing outgoing waves is adopted (Blayo and Debreu, 2005):

$$u_b = \pm\sqrt{\frac{g}{h}}\,(2\,\zeta_b - \zeta) \tag{13}$$

assuming that incoming and outgoing waves are perpendicular to the boundary. This type of radiation conditions has been shown to lead to good results with nearshore wave conditions. Here, u_{b} is the inflow velocity at the boundary and ζ_{b} is the surface elevation signal of the incident wave. The sign in (13) depends on the location of the boundary. The plus sign refers to an inflow velocity at the western and southern boundaries, and the minus sign refers to inflow velocity at the eastern and northern boundary. For regular waves, the incident signal can either be a time series or a Fourier series as given by

$$\zeta_{\mathrm{b}} = a_0 + \sum_{j=1}^{N} a_j \cos(\omega_j t - \varphi_j) \tag{14}$$

where N is the number of Fourier components, a_0 is the mean water level, and a_j, ω_j and φ_j are the amplitude, angular frequency and local phase lag, respectively, of the j^{th} component.

Irregular waves are usually treated as realisations of a stationary, Gaussian process which can readily be described by means of a Fourier series (Holthuijsen, 2007). We will restrict ourselves here to unidirectional waves, although SWASH allows to specify multidirectional waves as well. Using the linear wave theory, the velocity at a depth is found by linear superposition of N harmonic waves whose amplitude is determined by sampling a variance density spectrum and whose phase is randomly chosen for each realisation:

$$u_{\mathrm{b}}(z,t) = \sum_{j=1}^{N} a_j \left[\omega_j \frac{\cosh k_j(z+d)}{\sinh k_j h} + \sqrt{\frac{g}{h}}\right] \cos(\omega_j t - \alpha_j) \; - \sqrt{\frac{g}{h}}\,\zeta \tag{15}$$

where k_j and α_j are the wave number and random phase, respectively, of each frequency ω_j. Moreover, the frequency range is uniformly resolved with a frequency interval $\Delta\omega$, i.e. $\omega_j = j\Delta\omega$. The wave number and frequency are

related by the dispersion relationship, $\omega^2 = gk\tanh(kh)$, whereas the random phase at each frequency is uniformly distributed between 0 and 2π. Note that the boundary condition (15) is augmented with the radiation condition to minimize reflections at the offshore boundary.

For a given wave spectrum $E(\omega)$, a time series (15) can be synthesized by calculating the amplitude of each harmonic, as follows

$$a_j = \sqrt{2E(\omega_j)\Delta\omega} \tag{16}$$

The spectrum may be obtained from observations for the desired sea state or by specifying a parametric shape of the spectrum, such as the well-known Jonswap spectrum for fetch-limited conditions in deep water. Another fetch-limited spectrum is the so-called TMA spectrum that may be employed to generate waves characteristic of those occurring in shallower waters (Holthuijsen, 2007).

Finally, we may consider two types of onshore condition. The moving shoreline, in the case of inundation or runup computations, requires a numerical treatment which will be outlined in Section 3. If the onshore boundary is located in the pre-breaking zone, an absorbing condition may be imposed. Usually, the Sommerfeld's radiation condition is employed, which allows the (long) waves to cross the outflow boundary without reflections. For instance, for the case of a boundary parallel to $y-$axis, this condition is given by

$$\frac{\partial u}{\partial t} + \sqrt{gh}\frac{\partial u}{\partial x} = 0 \tag{17}$$

This radiation condition may be combined with a sponge layer technique; see Stelling and Zijlema (2003) for details.

3 Numerical implementation

The computational solutions to follow have been implemented in the SWASH code, recently developed at Delft University by the authors. This employs a finite difference method on a staggered, orthogonal curvilinear grid of the governing equations. The basic principles of this approach, as well as the underlying rationale for staggering locations pertaining to mass conservation and velocity components will be pursued here. For the sake of clarity these principles will be elucidated by means of the one-dimensional, depth-averaged shallow water equations in non-conservative form, as follows,

$$\frac{\partial \zeta}{\partial t} + \frac{\partial hu}{\partial x} = 0 \tag{18}$$

$$\frac{\partial u}{\partial t} + u\frac{\partial u}{\partial x} + g\frac{\partial \zeta}{\partial x} + \frac{1}{2}\frac{\partial q_{\mathrm{b}}}{\partial x} + \frac{1}{2}\frac{q_{\mathrm{b}}}{h}\frac{\partial(\zeta - d)}{\partial x} + c_f\frac{u|u|}{h} = \frac{1}{h}\frac{\partial}{\partial x}\left(h\nu_{\mathrm{t}}\frac{\partial u}{\partial x}\right) \tag{19}$$

$$\frac{\partial w_{\mathrm{s}}}{\partial t} = \frac{2q_{\mathrm{b}}}{h} - \frac{\partial w_{\mathrm{b}}}{\partial t}\,, \quad w_{\mathrm{b}} = -u\frac{\partial d}{\partial x} \tag{20}$$

$$\frac{\partial u}{\partial x} + \frac{w_{\mathrm{s}} - w_{\mathrm{b}}}{h} = 0 \tag{21}$$

The extension to the two-dimensional framework is tedious but otherwise straightforward. Furthermore, discretization in the vertical direction in which the computational domain is divided into a fixed number of terrain-following layers, the so-called multi-layered case, is extensively discussed in Zijlema and Stelling (2005, 2008).

We consider a regular 1D grid $\{x_{i+1/2}\,|\,x_{i+1/2} = i\Delta x\,,\ i = 0, ..., I\}$ with I the number of grid cells and Δx the length of the grid cell. The location of the cell centre is given by $x_i = (x_{i-1/2} + x_{i+1/2})/2$. A staggered grid convention is used in which the velocity component u and surface elevation ζ are located at

$i + 1/2$ and i, respectively. The staggered grid avoids de-coupling of the unknowns, which otherwise may cause non-physical oscillations in non-staggered (colocated) grids. The variables d, q_b, ν_t, w_b and w_s are all located at i. As a consequence, the water depth h is given in point i.

For the time integration an explicit leapfrog scheme in conjunction with a second order explicit time step for advection, a first order explicit time step for the viscosity term and a first order implicit time step for the non-hydrostatic part is used. This scheme as proposed by Hansen (1956) employs staggering in time. The velocity u is evaluated at a half time step $(n+1/2)\Delta t$, whereas the surface elevation at a whole time step $(n+1)\Delta t$, with Δt the time step and n indicating the time level $t^n = n\Delta t$. This variant of the leapfrog scheme shares with the classical leapfrog scheme the advantages of second order accuracy in time and no wave damping. In addition, it requires less storage and makes the algorithm easy to implement.

We start with a discretization of the momentum equation (19), as follows,

$$\begin{aligned}
&\frac{u_{i+1/2}^{n+1/2} - u_{i+1/2}^{n-1/2}}{\Delta t} + u_{i+1/2}^{n-1/2}\,(L_x u)_{i+1/2}^{n-1/2} + g\frac{\zeta_{i+1}^n - \zeta_i^n}{\Delta x} + \\
&\frac{q_{\mathrm{b},i+1}^{n+1} - q_{\mathrm{b},i}^{n+1}}{2\Delta x} + \frac{\left(\overline{q}_{\mathrm{b},i+1/2}^{x}\right)^{n+1}}{\left(\overline{h}_{i+1/2}^{x}\right)^{n}}\,\frac{\zeta_{i+1}^n - \zeta_i^n - d_{i+1} + d_i}{2\Delta x} + c_f\frac{u_{i+1/2}^{n+1/2}|u_{i+1/2}^{n-1/2}|}{\left(\overline{h}_{i+1/2}^{x}\right)^{n}} = \\
&\frac{\nu_{\mathrm{t},i+1}h_{i+1}^n(u_{i+3/2}^{n-1/2} - u_{i+1/2}^{n-1/2}) - \nu_{\mathrm{t},i}h_i^n(u_{i+1/2}^{n-1/2} - u_{i-1/2}^{n-1/2})}{\left(\overline{h}_{i+1/2}^{x}\right)^{n}\Delta x^2}
\end{aligned} \tag{22}$$

Note that the bottom friction term is approximated implicitly to enhance the robustness of the model. Furthermore, L_x is a finite difference operator to advection term and the over bar notation is used to denote averages, for

instance,

$$\overline{h}^{x}_{i+1/2} = \frac{1}{2}\left(h_i + h_{i+1}\right) \tag{23}$$

Concerning the approximation L_x, any appropriate finite difference scheme can be employed. We come back to this issue later.

Discretization of Eq. (18) yields

$$\frac{\zeta_i^{n+1} - \zeta_i^n}{\Delta t} + \frac{\hat{h}^n_{i+1/2} u^{n+1/2}_{i+1/2} - \hat{h}^n_{i-1/2} u^{n+1/2}_{i-1/2}}{\Delta x} = 0 \tag{24}$$

Note that the explicit time stepping is carried out by solving Eq. (22) before Eq. (24). The water depth $\hat{h}_{i+1/2}$ is not uniquely defined. An appropriate approximation is based on first order upwinding and is given by

$$\hat{h}_{i+1/2} = \begin{cases} \zeta_i + \min(d_i, d_{i+1})\,, & \text{if } u_{i+1/2} > 0 \\ \zeta_{i+1} + \min(d_i, d_{i+1})\,, & \text{if } u_{i+1/2} < 0 \\ \max(\zeta_i, \zeta_{i+1}) + \min(d_i, d_{i+1})\,, & \text{if } u_{i+1/2} = 0 \end{cases} \tag{25}$$

Based on this expression, it can be shown that if the time step is chosen such that $\Delta t |u^{n+1/2}_{i+1/2}|/\Delta x \leq 1$ at every time step then the water depth h_i^{n+1} is non-negative at every time step (Stelling and Duinmeijer, 2003). Hence, flooding never happens faster than one grid size per time step, which is physically correct. This implies that the calculation of the dry areas does not need any special feature. For this reason, no complicated drying and flooding procedures as described in Stelling (1983) are required. Additionally, the shoreline motion in the swash zone can be simulated in a natural manner. For computational efficiency, the momentum equation (22) is not solved and the velocity u is set

to zero if the water depth $\hat{h}_{i+1/2}$ is below a threshold value. Throughout this work, it equals 0.05 mm.

To achieve second order accuracy in space for the approximation of $\hat{h}_{i+1/2}$, we add a higher order interpolation augmented with a flux limiter:

$$\hat{h}_{i+1/2} \leftarrow \hat{h}_{i+1/2} + \begin{cases} \frac{1}{2}\Psi(r^{+}_{i+1/2})(\zeta_i - \zeta_{i-1})\,, & \text{if } u_{i+1/2} > 0 \\ \\ \frac{1}{2}\Psi(r^{-}_{i+1/2})(\zeta_{i+1} - \zeta_{i+2})\,, & \text{if } u_{i+1/2} < 0 \end{cases} \tag{26}$$

where

$$r^{+}_{i+1/2} = \frac{\zeta_{i+1} - \zeta_i}{\zeta_i - \zeta_{i-1}}\,, \quad r^{-}_{i+1/2} = \frac{\zeta_{i+1} - \zeta_i}{\zeta_{i+2} - \zeta_{i+1}} \tag{27}$$

are the upwind ratios of consecutive gradients of the surface elevation, and $\Psi(r)$ is the flux limiter to avoid unwanted oscillations near sharp gradients. For the test cases in this paper, the so-called MUSCL limiter (Van Leer, 1979) is employed, as given by

$$\Psi(r) = \max\left[0, \min\left(2, \frac{1}{2}r + \frac{1}{2}, 2r\right)\right] \tag{28}$$

which has been found to give the best results.

It is recalled that the momentum equation (19) is employed in the non-conservative form and thus, in principle, unable to conserve momentum. It should be clear that this formulation in conjunction with the widespread use of staggered grids is neccessitated by efficieny and accuracy for subcritical flows, see e.g. Stelling (1983). Shock-capturing schemes, designed for flow expansions, are usually Godunov-type schemes based on an approximate Riemann solver on colocated grids. They take characteristic features of the complete

set of conservation laws of mass and momentum into account. They aim, in particular, to mimic the so-called Riemann invariants propagation features implied by these conservation laws making them suitable for rapidly varied flows. However, they lack the desired efficiency of staggered schemes and can hardly be extended to three-dimensional non-hydrostatic flows. In Stelling and Duinmeijer (2003), a scheme is proposed that is momentum conservative while being applicable for staggered grids. The obvious advantage gained is that this efficient scheme is able to deal with flows with a wide range of Froude numbers. In addition, in the context of simulating wave dynamics, it ensures that the wave properties under breaking waves are modelled correctly. The manner in which the momentum conservation is achieved is one key facet of a successful implementation of the momentum equation into the staggered grid arrangement, and this is thus exposed below in some detail.

The following identity is used:

$$u\frac{\partial u}{\partial x} = \frac{1}{h}\left(\frac{\partial(\phi u)}{\partial x} - u\frac{\partial \phi}{\partial x}\right) \tag{29}$$

with $\phi \equiv hu$ the discharge. An appropriate approximation for this quantity is

$$\phi_{i+1/2} = \hat{h}_{i+1/2} u_{i+1/2} \tag{30}$$

A momentum-conservative advection scheme is given by

$$u_{i+1/2}\ (L_x u)_{i+1/2} = \frac{1}{\overline{h}^x_{i+1/2}}\left(\frac{\overline{\phi}^x_{i+1}\hat{u}_{i+1} - \overline{\phi}^x_i \hat{u}_i}{\Delta x} - u_{i+1/2}\,\frac{\overline{\phi}^x_{i+1} - \overline{\phi}^x_i}{\Delta x}\right) \tag{31}$$

To retain second order accuracy in time, this scheme is combined with the well-known MacCormack predictor-corrector technique, which includes two

steps in each time step. In the predictor step, Eq. (22) is replaced by

$$\frac{u^*_{i+1/2} - u^{n-1/2}_{i+1/2}}{\Delta t} + u^{n-1/2}_{i+1/2}\ (L_x u)^{n-1/2}_{i+1/2} + ... + c_f \frac{u^*_{i+1/2}|u^{n-1/2}_{i+1/2}|}{\left(\overline{h}^x_{i+1/2}\right)^n} = ... \tag{32}$$

to obtain an intermediate value u^*. In this step, the first order upwind scheme is used to approximate $\hat{u}$ at point i:

$$\hat{u}_i = \begin{cases} u_{i-1/2}\ , \text{ if } \overline{\phi}^x_i \geq 0 \\ \\ u_{i+1/2}\ , \text{ if } \overline{\phi}^x_i < 0 \end{cases} \tag{33}$$

In the corrector step, the predicted value u^* is corrected according to

$$u^{n+1/2}_{i+1/2} = u^*_{i+1/2} - \frac{\Delta t}{\left(\overline{h}^x_{i+1/2}\right)^n} \left(\frac{\left(\overline{\phi}^x_{i+1}\right)^{n-1/2} \Delta u_{i+1} - \left(\overline{\phi}^x_i\right)^{n-1/2} \Delta u_i}{\Delta x} \right) \tag{34}$$

with

$$\Delta u_i = \begin{cases} \frac{1}{2}(u^*_{i-1/2} - u^{n-1/2}_{i-3/2})\ , \text{ if } \left(\overline{\phi}^x_i\right)^{n-1/2} \geq 0 \\ \\ \frac{1}{2}(u^{n-1/2}_{i+1/2} - u^*_{i+3/2})\ , \text{ if } \left(\overline{\phi}^x_i\right)^{n-1/2} < 0 \end{cases} \tag{35}$$

With this second order correction, the one-sided second order backward difference (BDF) scheme is obtained. This upwind scheme generates a limited amount of numerical dissipation which is sufficient to avoid spurious waves with wave length of $2\Delta x$ effectively.

The time integration is of explicit type and thus requires strict confirmity of stability criteria for a stable solution. The well-known CFL condition is given

by

$$\mathrm{Cr} = \frac{\Delta t \left(\sqrt{g \left(\overline{h}^{x}_{i+1/2} \right)^{n+1}} + |u^{n+1/2}_{i+1/2}| \right)}{\Delta x} \leq 1 \tag{36}$$

with Cr the Courant number evaluated at a velocity point. A dynamically adjusted time step controlled by the Courant number is implemented in SWASH as follows. The actual maximum of the Courant number over all wet grid points is determined. The time step is halved when this number becomes larger than a preset constant $\mathrm{Cr}_{\max} < 1$, and the time step is doubled when this number is smaller than another constant $\mathrm{Cr}_{\min}$, which is small enough to be sure the time step can be doubled. In all the numerical computations presented here, $\mathrm{Cr}_{\min}$ is set to 0.1, while the maximum Courant number $\mathrm{Cr}_{\max}$ will be specified differently for different cases.

The explicit treatment of the viscosity term of Eq. (22) leads to the following additional stability condition:

$$\Delta t \leq \frac{\Delta x^2}{2\nu_{\mathrm{t}}} \tag{37}$$

This time step restriction is typically very local but often more severe compared to the CFL condition (36). To overcome this stringent limitation, the model adopts a constraint, which a maximum of the eddy viscosity is determined at each time step, as follows

$$\nu_{\mathrm{t}} = \min \left(\nu_{\mathrm{t}}, \frac{\Delta x^2}{2\Delta t} \right) \tag{38}$$

This clipping of the eddy viscosity only happens occasionally in terms of a few percentage of the total active grid points.

Hitherto, a numerical framework for solving the shallow water equations has been discussed. There remains the question of how to determine the non-hydrostatic pressure q_{b} appearing in Eqs. (19) and (20). Since this pressure is governed, indirectly, by the local continuity equation (21), attention must focus on this equation and its linkage to the momentum equations. A common approach to establishing such a linkage is the so-called pressure correction technique. The second order method given in Van Kan (1986) is employed. This is based on combining the discretized forms of the continuity and momentum equations (21), (19) and (20) to give a Poisson equation linking the non-hydrostatic pressure correction at a grid point to its neighbours. As a result, local mass conservation is enforced. This technique is extensively outlined in Zijlema and Stelling (2005). We use either SIP (Stone, 1968), in the case of depth-averaged mode, or BiCGSTAB (Van der Vorst, 1992) preconditioned with an ILU, in the case of multi-layered mode, for the solution of the Poisson equation. Further details on this subject can be found in Zijlema and Stelling (2005).

4 Parallelization strategy

The scale of the typical two-dimensional applications dictates that the serial code of SWASH must be implemented for parallel computers, since the run times on a present-day single processor can be range from hours to days. Parallel simulation using multiple processors is frequently used to overcome such a limit. Obtaining good scalability for relatively large number of processors is usually achieved through distributed memory machines with each processor having its own private memory. The conventional methodology for paralleliza-

tion on distributed computer systems is domain decomposition, which not only benefits from carrying out the task simultaneously on many processors but also enables using a large amount of memory. It gives efficient parallel algorithms and is easy to program within message passing environment (e.g. MPI).

A stripwise grid partitioning is employed. It is based upon a partition of the whole computational domain into a number of strips, along the $x-$ or $y-$axis, with each of them being assigned to a different processor. However, in the context of SWASH applications to coastal areas, some difficulties arise. Firstly, wet and dry grid points may unevenly distributed over subdomains while no computations have to be done in dry grid points. And secondly, a load imbalance may arise during the simulation due to flooding and drying e.g. by swash motions. In such cases, one may decide to repartition such that they are balanced again. For the time being, however, we restrict ourselves to balanced, static grid partitions.

Each subdomain can have multiple neighbors on each of its sides. For this, a data structure is implemented to store all the information about the relationship of the subdomain and its particular neighbors. Next, each subdomain, look at in isolation, is surrounded by an auxiliary layer of three grid points width originating from neighboring subdomains. This layer is used to store the so-called halo data from neighboring partitions that is needed for the solution within the subdomain in question. Since, each processor needs data that reside in other neighboring subdomains, exchange of data across subdomains is necessary. Moreover, to evaluate the stopping criterion of the iterative solution methods for pressure correction (SIP, preconditioned BiCGSTAB), global communication is required as well. These message passings are implemented

by a high level communication library MPI. Only simple point-to-point and collective communications have been employed.

The most difficult part of the program to parallelize is the iterative solution method, since it usually contains recurrence relations. One approach suggested in the literature (Barrett et al., 1994) consists of treating the data on the subdomain interface explicitly, i.e. taking the solution from the previous time step located in the halo cells. This method possesses a high degree of parallelism, but may lead to a certain degradation of convergence properties. From many experiments this approach appeared to be the best one for the ILU-preconditioned BiCGSTAB method. For the SIP method, however, another parallelization strategy has been chosen. It is based on a so-called wavefront approach. The rationale behind this approach is that the pressure correction unknowns on a diagonal of the grid only depend on the unknowns corresponding to the previous diagonal. As such, all unknowns corresponding to the same diagonal can be computed independently. This facilitates parallelization. This approach does not alter the order of computing operations of the sequential algorithm and thus preserves the convergence properties, but reduces parallel efficiency to a lesser extent because of the serial start-up and shut-down phases. For details, see Barrett et al. (1994).

5 Some illustrative applications of SWASH

This section aims to convey the capabilities of SWASH by presenting calculations for seven test cases for which experimental data have been obtained under well-controlled laboratory conditions. In addition, four cases have been included for which analytical solutions are provided, to verify numerical ac-

curacy of some distinct features of the model, namely frequency dispersion, shock capturing and wetting and drying. While none of these cases considered here relates directly to real-life applications, the wave and flow features considered are generic and expected to be encountered in most nearshore-related applications.

These eleven cases have been chosen so as to cover a broad range of wave and flow conditions and computational challenges. In addition, for the presentation, they have been ordered by level of difficulty. Physical issues arising from the performance of SWASH with respect to proper conservation properties in case of transitions from super- to subcritical flow (hydraulic jump), flooding and drying in case of wave runup on a island and N-wave runup on a complex beach, cross-shore motions of irregular breaking waves, surf beats, nearshore circulations and setups induced by breaking waves are discussed in some detail. The examples selected are drawn from those generated by the authors. A complementary set of test cases has been reported by Stelling and Zijlema (2003), Stelling and Duinmeijer (2003), Zijlema and Stelling (2005,2008), Kramer and Stelling (2008) and Cui et al. (2010).

5.1 Linear progressive waves through a flume

The purpose of this test is to validate the model capability for resolving frequency dispersion in an accurate manner by means of progressive waves. Simulating progressive waves is more demanding compared to standing waves in a closed basin which is a quite common test case for verifying the accuracy of linear dispersion. The difficulty lies in the fact that the orbital velocity under a wave crest reach its maximum value and not zero as for standing waves, and

thus progressive waves form a very suitable test case for SWASH.

We consider a linear progressive wave propagating through a flume with a length of 36λ, with λ the wave length. A weakly reflective hyperbolic cosine distribution of velocity in the vertical based on linear wave theory was imposed at the inlet of the flume. A combination of a sponge layer with a width of two wave lengths and the Sommerfeld's radiation condition was applied at the outlet to minimize wave reflection. Five different cases were carried out; wave amplitude a_0, wave period T_0 and still water depth d are such that $kd = \pi$, $kd = 2\pi$, $kd = 3\pi$, $kd = 4\pi$ and $kd = 5\pi$, respectively, and in all cases $a_0/d = 0.001$. For these cases, a grid size of $\Delta x = \lambda/30$ was employed, whereas the time step was specified during the simulation by a maximum Courant number of 0.5. To optimize wave dispersion and to resolve vertical velocity profile properly, the following vertical layer distributions for the considered cases have been employed. For the first case, $kd = \pi$, two equidistant layers were chosen, for the second case, $kd = 2\pi$, three equidistant layers were taken and for the remaining cases, three non-equidistant layers were specified with the following thicknesses: 10%, 20% and 70% of the total depth for top, middle and bottom layer, respectively. In Figure 1, the numerical results for the surface elevation at $x = 30\lambda$ are compared to the analytical solutions. Clearly, the model is able to capture the wave dispersion in intermediate and deep waters effectively using a few number of vertical layers. Only for the last two cases, $kd = 4\pi$ and $kd = 5\pi$, the predicted wave propagates slightly faster after a relatively long distance of a few tens of wave lengths.

5.2 Tidal wave flow over an irregular bed

We consider a tidal wave flow over an irregular bottom for which an asymptotic solution is derived by Bermudez and Vazquez (1994). Their derivation makes use of the NLSW equations in strong conservation form with a space-varying bottom elevation. They showed the paramount importance of an accurate and robust approximation of the bed slope source term in order to avoid numerical parasitic waves. Similar results have been found in, e.g. Zhou et al. (2001) and Wei et al. (2006).

A tidal wave with 4 m height and 12 hour period propagates in a one dimensional channel with a length of $L = 14$ km and a variable depth as given by

$$d(x) = 50.5 - \frac{40\,x}{L} - 10\,\sin\left[\pi\left(\frac{4\,x}{L} - \frac{1}{2}\right)\right] \tag{39}$$

Both the water level and flow velocity are initially set to zero. The boundary conditions are

$$\zeta|_{x=0} = 4 - 4\,\sin\left[2\pi\left(\frac{t}{43,200} + \frac{1}{4}\right)\right], \quad u|_{x=L} = 0 \tag{40}$$

The asymptotic solution is given by

$$\zeta(t) = 4 - 4\,\sin\left[2\pi\left(\frac{t}{43,200} + \frac{1}{4}\right)\right] \tag{41}$$

$$u(x,t) = \frac{\pi(x-L)}{5400\,(\zeta(t) + d(x))}\,\cos\left[2\pi\left(\frac{t}{43,200} + \frac{1}{4}\right)\right] \tag{42}$$

From Eq. (41) it is clear that the surface elevation is a function of time only.

The results of the numerical simulation, with $\Delta x = 280$ m, at $t = 7552.13$

s are shown in Figure 2. Good agreement is obtained between the numerical and asymptotic solutions. Yet, no spatial variation in the predicted water level is encountered, i.e. the present model does not exhibit artificial waves. This suggests that SWASH applies the correct conservation properties.

5.3 Tsunami wave runup on a plane beach

This case is a good example of the benefits of assuring non-negative water depths when flooding and drying is involved. A leading depression N-wave is let to runup and rundown on a sloping beach. This situation has an analytical solution derived from the NLSW equations by Carrier et al. (2003). The initial free surface is formed by an N-wave shape as proposed theoretically by Carrier et al. (2003). This profile resembles a tsunami wave typically caused by a submarine landslide.

We have considered a numerical flume of 1 km wide, 50 km long, with a uniformily sloping bed. The still water depth at the toe of the slope was 5000 m, while the slope equaled 1:10. The calculation was carried out using a non-uniform grid with a higher grid resolution during runup and rundown to better capture moving shoreline. Additionally, the time step was kept constant at 0.01 s, whereas the maximum Courant number was 0.2. Figure 3 presents the predicted water levels at 3 different times, along with the analytical surface elevations. The comparison between numerical and analytical shoreline movement is shown in Figure 4. The model correctly reproduces both the runup and moving waterline, thereby indicating that the proposed wet-dry algorithm is accurate for runup of a tsunami event.

5.4 Long wave resonance in a circular parabolic basin

An analytical solution of the NLSW equations in two horizontal dimensions is due to Thacker (1981). This relates to a long wave resonating in a circular parabolic basin and includes the moving shoreline implicitly. This case provides a severe test problem for the model and has been featured in numerous papers as well. Examples of these include Lynett et al. (2002), Wei et al. (2006) and Fuhrman and Madsen (2008).

The frictionless flow takes place inside a parabolic basin with the following shape

$$d(x,y) = d_0\left(1 - \frac{r^2}{R^2}\right) \tag{43}$$

with $r = \sqrt{x^2+y^2}$ the distance from the origin, d_0 the still water depth in the origin and R the radius of the still water level. The surface elevation is given by

$$\zeta(r,t) = d_0\left[\frac{\sqrt{1-A^2}}{1-A\cos\,\omega t} - 1 - \frac{r^2}{R^2}\left(\frac{1-A^2}{(1-A\cos\,\omega t)^2} - 1\right)\right] \tag{44}$$

where

$$A = \frac{R^4 - r_0^4}{R^4 + r_0^4} \tag{45}$$

with r_0 the initial wet radius, and

$$\omega = \frac{\sqrt{8gd_0}}{R} \tag{46}$$

the resonance frequency.

We replicate the test performed by Lynett et al. (2002) with d_0 =1 m, r_0 = 2,000 m and R = 2,500 m. The basin is 8,000 m wide, 8,000 m long, and was discretized with a uniform grid spacing of 20 m. The simulation was carried out using an initial time step $\Delta t = T/480$ with T the resonance period. The maximum Courant number was set to 0.3. The initial water level was taken from Eq. (44) with t =0, whereas the initial flow velocity was set to zero. Figure 5 plots the computed and exact surface elevations after the first period. The comparison indicates good agreement and shows the validity of the wet-dry procedure in a two-dimensional setting. It should be noted that the results become less accurate after a few cycles due to the numerical dispersion. A similar observation has been found earlier in Lynett et al. (2002) and Fuhrman and Madsen (2008).

5.5 Hydraulic jump in an open channel

A hydraulic jump is formed whenever supercritical flow changes to subcritical flow. In this transition, free surface rises abruptly, turbulent mixing occurs and energy is dissipated. We evaluated the ability of SWASH to predict the hydraulic jump in an open channel flow. The channel dimensions and flow parameters for this test case are identical to those used by Zhou and Stansby (1999). The channel of 30.5 m long consists of two parts with different slopes. The first one is horizontal and 14.5 m long, and the second is 16.0 m with a slope of 0.03; see Figure 6. The inflow is supercritical with a Froude number $\mathrm{Fr} = u/\sqrt{gh}$ of 4.65. The flow pass through a subcritical state followed by the critical depth (Fr =1) where a hydraulic drop occured, and becomes uniform and supercritical again at the downstream end.

The computational grid is one dimensional and consists of 60 equidistant grid cells. The initial water level and flow velocity are 0.06 m and 0 m/s, respectively, throughout the channel. At inlet, an ingoing Riemann invariant, defined as $u+2\sqrt{gh}$, of 5.105 m/s is specified, whereas at outlet, $\partial h/\partial x = 0$ is imposed. A Manning's roughness coefficient $n = 0.019$ is employed. The numerical result is depicted in Figure 6 and is comparable to that reported by Zhou and Stansby (1999). This figure illustrates all the essential features of the hydraulic jump. To verify the correctness of the computation, the well-known Bélanger formula is employed and is given by

$$\frac{h_1}{h_0} = \frac{-1 + \sqrt{1 + 8\mathrm{Fr}^2}}{2} \tag{47}$$

which express the ratio of the flow height after the jump, h_1, and just before the jump, h_0, depending on the upstream Froude number. From the numerical results, it follows that h_0 =0.1102 m and h_1 =0.2194 m, giving a ratio of 1.99. The Froude number just before the jump appears to be 1.78 implying a ratio of 2.07 according to Eq. (47). This gives a relative error of 4% which is acceptable.

5.6 Runup of solitary waves on a conical island

Briggs et al. (1995) conducted a laboratory experiment for solitary wave runup around a conical island. A physical test of this conical island has been set up in the centre of a 25 m long and 30 m wide basin. The shape of the island is a truncated circular cone with diameters of 7.2 m at the toe and 2.2 m at the crest. The height of the island is 0.625 m, whereas the slope is 1:4. The still water depth d of the basin is 0.32 m. Figure 7 depicts schematic views of the experiment, where the locations are indicated for comparison of the free

surface elevation.

Solitary waves with three different measured wave heights were generated at the western sidewall: $H = 0.045d$, $H = 0.096d$ and $H = 0.181d$. At the eastern boundary the Sommerfeld's radiation condition was applied, whereas the lateral sidewalls were modelled as fully reflected boundaries. The simulations were considered to be non-hydrostatic and depth-averaged. No bed roughness was assumed. Wave breaking occurs mainly on the lee side of the island for $H = 0.181d$ as demonstrated by Lynett et al. (2002). For this case, a mixing length of ℓ_m of 0.06 m was chosen. A uniform grid of 500×600 cells ($\Delta x = \Delta y = 0.05$ m) was employed. The initial time step was 0.01 s whereas the maximum CFL was set to 0.8. The simulation period was set to 25 s for all cases, while computations were run for 2500 time steps for cases $H = 0.045d$ and $H = 0.096d$, and 2515 time steps for the most severe case $H = 0.181d$.

Figure 8 shows the time series of the computed and measured surface elevations at selected gauges for the different wave conditions considered. The agreement with experimental data is satisfactory. Generally, both the arrival time and the wave height of the primary wave are adequately reproduced. Also, the depression following the leading wave is captured well, albeit with some phase differences. Similar results have been obtained elsewhere using Boussinesq-type wave models as discussed in Lynett et al. (2002) and Fuhrman and Madsen (2008), a finite-volume, depth-averaged NLSW model of Wei et al. (2006) and a depth-averaged non-hydrostatic model of Yamazaki et al. (2009). For $H = 0.181d$, the soliton breaks on the backside of the island where the trapped waves collide. The present model appeared to predict the leading wave height at gauge 22 correctly, although there is a small deviation in the phase of the peak. Yet, it is worth emphasising the value of momentum conservation in

conjunction with the Prandtl mixing length hypothesis in capturing breaking waves. As final validation, the maximum horizontal runup around the island is compared to the measured one; see Figure 9. Clearly, the inundation position is predicted reasonably well at the front, side, and rear of the island, and the agreement is similar to that achieved in the aforementioned cited references. A minor discrepancy occurs around the front of the island for the most steepest case, $H = 0.181d$, where the runup is slightly underpredicted.

Finally, a few words about the computational efficiency of the SWASH model. The execution time needed for the case $H = 0.181d$ appeared to be about 28 CPU minutes on a single 2.0 GHz Intel Core 2 processor, with the highest level of resource required by the solution of the pressure Poisson equation. This implies that the total CPU time per grid point and per time step required is about 2.2 μs.

The parallel performance of the SWASH model was measured on a dedicated Linux cluster with 8 nodes, each of which has 2 dual-core 64-bit AMD processors (1.8 GHz, 4MB L2 cache), and thus having a total of 32 computational cores. Each node contains 4 GB of memory that is shared among the cores, while the nodes are connected via Gigabit ethernet. Wall clock times in seconds were measured for the total execution including MPI communication. Usually, the performance of a parallel computation is measured by the speedup and efficiency. The speedup S_p is defined as the ratio between the turnaround time needed by 1 computational core and by p computational cores. The efficiency, as measure for scalability, is determined by $E_p = S_p/p$. The performance test was conducted for 1, 2, 4, 8, 12, 16 and 32 cores. The measured timings, speedups and efficiencies are reported in Table 1. Clearly, the model shows super linear scaling up to 12 cores, but then it levels off. At this point, the

communication overhead slows down the parallel performance. Still, the computing time for this particular simulation has been reduced to about 80 ns per grid point and per time step. Possible causes for observed super linear speedup are memory sharing and cache effect.

5.7 N-wave runup on a complex beach

The Hokkaido Nansei-oki tsunami of 1993 produced unexpectedly large runup heights in Monai Valley, Japan. The maximum runup height was over 30 m, whereas an average of 24 m runup height was observed along the beach (Matsuyama and Tanaka, 2001). To study this unusual phenomenon, Matsuyama and Tanaka (2001) conducted a laboratory experiment for N-wave transformation and runup in a large-scale flume of 205 m long, 3.4 m wide and 6 m deep. The bathymetry of this 1:400-scale laboratory model with a small pocket beach is partly shown in Figure 10. Complete time series of measured surface elevation were provided at three wave gauges behind Muen Island as indicated in the figure. Also the measurements of some runup heights in the pocket beach, including the highest one, were available.

For the present simulation the numerical setup of Yamazaki et al. (2011) has been taken. The numerical basin is 5.475 m long and 3.4 m wide. A uniform grid was chosen with $\Delta x = \Delta y = 0.0125$ m, while an initial time step of 0.005 s was taken with a maximum Courant number of 0.5. The simulation period was set to 30 s. At the western boundary an N-wave, as shown in Figure 11, was imposed. A Manning's roughness coefficient $n = 0.012$ was used. The simulation was depth-averaged and non-hydrostatic of nature.

Figure 12 presents the comparison of the computed surface elevation with measured data at different gauge locations. Both the amplitude and phase of the first wave are predicted very well. Similar results have been found in Cui et al. (2010) and Yamazaki et al. (2011). Matsuyama and Tanaka (2001) have measured runup heights along transects at $y = 2.2062$ and $y = 2.32$ m as well as the maximum value inside Monai Valley from a series of tests. These recorded runup data with some spreading can also be found in Table I of Yamazaki et al. (2011). Figure 13 shows the computed runup with the range and sample mean of the measured runup. Despite the uncertainty in the measured data the computed runup heights agree well with the measured ones, particularly the one at Monai Valley where the highest runup has been observed. This is consistent with the findings of Yamazaki et al. (2011).

5.8 Irregular waves breaking on a bar-trough beach profile

The laboratory flume test of Battjes and Janssen (1978) is considered, in which random, uni-directional waves propagate towards a bar-trough profile (see Figure 14). Battjes and Janssen (1978) considered five different conditions applied to the bar-trough beach of which two of them will be discussed in this paper: mildly breaking (run 13 of Battjes and Janssen) and strongly breaking (run 15). The incident significant wave height H_{m0} and peak period T_p are given as 0.147 m, 2.01 s and 0.202 m, 1.89 s, respectively. In both cases, a one-dimensional Jonswap spectrum was imposed. The grid size was set to 0.05 m and the time step was taken initially as 0.005 s with a maximum Courant number of 0.5. The computations considered were depth-averaged. The mixing length ℓ_m used in these calculations was 0.15 m and 0.20 m, respectively. At

outflow, a sponge layer of typically two incident wave lengths in conjunction with the Sommerfeld's radiation condition was given. For comparison, SWAN computations have been included as no measured energy density spectra were available. The default surf zone physics of SWAN has been employed, namely the depth-induced wave breaking model of Battjes and Janssen (1978) and the Lumped Triad Approximation (LTA) for nonlinear interactions (Holthuijsen, 2007) [2]. A well-known deficiency of LTA is the overestimation of the first superharmonic (Becq-Girard et al., 1999). Moreover, only sum interaction is considered while the generation of low-frequency (lf) motion ('surf beat') is excluded.

Figure 15 displayed the wave height along the flume for both cases. The predicted wave heights are overall in good agreement with observations. Figure 16 demonstrates the comparison of SWASH- and SWAN-computed wave spectra at different locations in the flume. As expected, the generation of the first superharmonic has been prevailed in the SWAN-computed spectra, while the subharmonics are completely lacked. By contrast, the spatial evolution of the SWASH-computed spectral levels is characterized by increases of energy at lower and higher frequencies, while lowering the peak frequency, qualitatively consistent with the well-known triad interaction rules. Moreover, because of the interplay between depth-induced wave breaking and triad nonlinear interaction occurring in the surf zone, the spectrum evolves from relatively peaked at the offshore location to a broad, flat one at nearshore positions. These findings illustrate the first-principle based model representations of the relevant nearshore processes.

[2] Bottom friction was not included.

5.9 Irregular wave breaking in a barred surf zone

The case considered is the laboratory flume experiment of Boers (1996) which features a barred beach; see Figure 17. Here the wave condition 1B from Boers (1996) is discussed, determined by a prescribed spectrum with parameters H_{m0} = 0.206 m and T_p = 2.03 s. This wave field is energetic and has a relatively high mean steepness, and at the inflow already has a reasonable amount of energy at superharmonic frequencies. Moreover, spilling breakers have been observed throughout the wave flume.

The considered case was simulated with SWASH using the following settings. The calculation was run in the depth-averaged mode with a grid size of 0.02 m and the time step was taken initially as 0.001 s. The maximum Courant number was set to 0.5 and the simulation time equaled 1680 s. The mixing length ℓ_m was taken to be 0.13 m (which appears to be optimal for other wave conditions of the experiments of Boers (1996) as well). At outflow, the Sommerfeld's radiation condition was applied.

Figure 18 shows that the energy levels at superharmonic frequencies decrease steadily, as the waves propagate towards the shore, due to breaking dissipation. Meanwhile, the steady growth in the spectral levels at the low-frequency range due to difference triad interaction is clearly observed. Also, the further inshore the broader the spectrum shape, which is attributed to the nonlinear couplings and wave breaking. From this figure we see overall good agreement between model predictions and observations. Figure 19 presents the integral wave parameters. The significant wave height is somewhat underestimated offshore of the first breaker bar and slightly overpredicted in between the bars,

presumably due to over and under dissipation, respectively. In the swash zone, however, model-predicted wave heights agree well with the measurements. The calculated zero-crossing period T_{m02} is slightly overpredicted throughout the flume. Nevertheless, the qualitative trend of the mean period is well resolved by the model.

5.10 Wave transformation over a shallow foreshore

In Van Gent and Doorn (2000) physical and numerical model studies have been performed to model wave propagation over a shallow foreshore with a bar. A prototype of this foreshore at the Petten Sea defence at the Dutch coast has been set up in a wave flume at a scale of 1:40; see Figure 20. The measurements included 20 different wave conditions of which 6 of them correspond to storm conditions and the other 14 ones are idealised to study the influence of several parameters like wave height, wave steepness, spectral shape and water level.

Numerical simulations were carried out using a grid size of 1.0 m, an initial time step of 0.02 s and 2 equidistant layers. A simulation period of 60 minutes has been chosen so as to obtain a steady-state solution while the Courant number was set to 0.5. Measured wave spectra at the start of the foreshore were imposed as incident frequency spectra. In the cases with storm conditions, full wave reflection near the toe has been incorporated in the computations, since long wave reflection at the shoreline has been observed. In the other simulations the radiation condition of Sommerfeld has been applied at the outflow boundary in order to minimize wave reflections.

Figure 21 illustrates the comparison of measured and computed wave spectra

at different locations (see Figure 20) for a storm condition (test 1.04 of Van Gent and Doorn (2000); incident parameters: $H_{m0} = 4.4$ m, $T_p = 16.2$ s at a water level of 1.7 m). The numerical simulation shown in this figure uses $\ell_m = 4$ m. The model-predicted spectral evolution is generally in good agreement with the observations. At low frequencies, long waves including reflected components are generated while the amount of energy in the short waves decreases. Also notable is the fact that the shape has been broadened. These findings are in line with what was discussed in the test cases presented earlier.

Another testcase is an idealised case with a relative high wave steepness (test 2.51; incident 1D Jonswap spectrum with $H_{m0} = 6$ m and $T_p = 9$ s at a water level of 4.7 m) of which the results are depicted in Figure 22. (The mixing length was set to 3 m.) It demonstrates clearly the strong response of the peak energy levels to high steepness in which those levels are attenuated and nonlinear three-wave transfer accros the frequencies is very limited. Again, good agreement to observations is found.

5.11 Wave-induced nearshore circulation on a barred beach with rip channels

Although rip currents and their effects on nearshore circulation have been observed in the field for many years, there are quite a few laboratory data involving rip currents on a longshore varying bathymetry, of which Haller et al. (2002) is the most comprehensive one so far. These data were obtained in a directional wave basin with a longshore, submerged bar where two rip channels were present. The experiment was carried out using regular waves only. Wave-driven currents, wave heights and setups were measured over a large area of the basin to get a detailed picture of the rip current circulations.

Earlier numerical studies related to this rip current system have been carried out by Chen et al. (1999) and Haas et al. (2003).

Comparisons with the observations of test B from Haller et al. (2002) are considered. The corresponding wave condition is a monochromatic, normally incident wave with a height of 4.75 cm and a period of 1 s. The bottom topography used in the present simulations is depicted in Figure 23, where two rip channels incising a bar are clearly shown. The computational domain is 13.05 m long and 18.2 m wide. The seaward boundary is located at the most offshore wave gauge, which is at 3.95 m from the wave maker, thus giving a more precise forcing of the model. The offshore still water depth is 0.374 m, while the beach slope is 1:30. A discharge was imposed at the seaward boundary, which is uniform alongshore. This discharge is determined by means of the linear wave theory given the wave condition. The radiation condition was imposed at the shoreline to minimize reflections. The lateral boundaries were closed. A simulation was carried out using a uniform grid with $\Delta x = \Delta y =$ 0.05 m, an initial time step of 0.01 s, and a maximum Courant number of 0.8. A single layer was considered to be enough. Exactly 163,800 time steps were needed to complete the simulation period of 1638 seconds, which is the duration of the considered physical test as well. Since, wave breaking causes a forcing on the mean current, while this force balances bottom friction and lateral turbulent mixing, a Manning's roughness coefficient $n = 0.017$ and a mixing length $\ell_m = 3$ cm were adopted. These values were determined by calibration. Note that turbulent mixing is implicitly accounted for in the Prandtl mixing length hypothesis, although its effect is usually small compared to that of wave breaking. Thus, the effective mixing length is somewhat smaller than the given value of 3 cm.

The cross-shore variation of the measured and computed wave height and setup over the center bar ($y = 11.23$ m) and along the centerline of the rip channel ($y = 13.68$ m) are shown in Figures 24 and 25, respectively. Obviously, both wave breaking and the wave setup are fairly captured by the model. Moreover, waves over the bar break earlier than those through the channel. This creates an alongshore variation of the mean water level close to the shore and subsequently drives a circulation pattern. Figure 26 presents a comparison between the measured and computed mean cross-shore current along five longshore sections. These are close to the shoreline ($x = 14$ m), in the trough behind the bar ($x = 13$ m), over the bar ($x = 12.2$ m), on the offshore edge of the bar ($x = 11.2$ m), and 1 m offshore of the bar ($x = 10$ m). The agreement is fairly good for all the sections. In particular, at both sides of the bar, the model captures well the important details of the longshore variation of the cross-shore velocity. The longshore variation of the mean longshore current from the simulation compared to the measured one along the five transects is seen in Figure 27. Again, model predictions are in overall good agreement with the observations. The quality of these predictions is similar to the ones found in Chen et al. (1999) and Haas et al. (2003).

The considered simulation was very compute intensive; it taked about 9 CPU hours on a single 2.0 GHz Intel Core 2 processor to complete the run. In other words, for a simulation of an hour of real time it requires approximately 20 hours of computing time. This clearly shows the need for parallelism. Numerical computations have been carried out for the full simulation period on 1 through 32 computational cores of the Linux cluster mentioned in Section 5.6. The computing times and speedup factors for these runs are shown in Table 2. These results show a super linear speedup of up to a factor 8.6 on 8

cores, which is obtained through a reduction of simulation time by memory sharing among the cores combined with effective cache utilisation that is more substantial than the communication overhead. However, at higher numbers of computational cores, the parallel efficiency is being reduced as the communication begins to dominate the computation time. Nonetheless, this efficiency is larger than 65%, indicating that the parallel algorithm is rather scalable to larger numbers of computational cores. Note that the computing time has been reduced to less than 45 minutes per hour to be simulated. Also, the required CPU time on 32 cores amounted to about 76 ns at each grid point on each time step.

6 Concluding remarks

The paper has given a detailed exposition of the main elements of the public domain SWASH model for simulating non-hydrostatic, free-surface, rotational flows in one and two horizontal dimensions. This model stands out in its ability to simulate complex nearshore processes, including wave breaking, nonlinear interaction, wave runup and wave-induced circulation. A further distinguishing feature is the numerical implementation of momentum conservation, which is a prerequisite for a plausible representation of hydraulic jumps and bores. The computational algorithm combines efficiency and robustness allowing application to large-scale, real-life problems. In addition, the turnaround time of this algorithm can be effectively reduced by means of parallelism. The resulting code can be executed on computer clusters making use of an arbitrary number of computational cores. Performance experiments reveal good run time reduction and have illustrated the viability of the parallelization strategy followed

in SWASH.

The examples included not only demonstrate the capabilities of the SWASH model, but also expose a number of interesting physical issues. For instance, it was shown that this model with three non-equidistant vertical layers exhibits accurate wave dispersion up to $kd \approx 16$ when linear progressive waves are involved. However, using two equidistant layers would be adequate to retain accurate propagation of progressive waves for $kd \leq 3$, typically occurring in most nearshore applications.

Considering a typical surf zone where the dominant processes of triad interaction and depth-induced breaking can be isolated, it was found that the model yields a realistic representation of the observed frequency spectra, including the overall spectral shape at frequencies above the spectral peak, and the inclusion of subharmonics. This is followed by a transformation toward a broadband spectral shape as the waves approach the shoreline. Accordingly, the integral wave parameters are also predicted well. Such phenomena appear to be rooted in the ability of the momentum-conservative scheme to mimic the dynamics within travelling bores associated with wave breaking across the surf zone. In addition, the comparison of numerical results with experiments shows the usefulness of the Prandtl mixing length hypothesis in situations of practical interest including severe wave breaking. Wave-induced nearshore circulation on a barred beach incised by rip channels has been studied as well, showing the potential of the model to reproduce adequately the variation of the wave heights, the wave setup and the wave-driven currents.

Finally, we believe that SWASH is very likely to be competitive with the extended Boussinesq-type wave models in terms of robustness and the computa-

tional resource required to estimate wave and flow quantities to an appropriate accuracy. In particular, the model improves its frequency dispersion by increasing the number of vertical layers rather than increasing the order of derivatives of the dependent variables like Boussinesq-type wave models. Yet, it contains at most second order spatial derivatives, whereas the applied finite difference approximations are at most second order accurate in both time and space. Moreover, the use of second order upwinding in the momentum equations effectively eliminates short wave instabilities and so, the model results remain stable without any artificial filtering. Additionally, SWASH requires just one tuning parameter for wave breaking, which in practice is relatively easy to estimate. Lastly, SWASH utilizes a simple and numerically stable procedure yielding non-negative water depths with which an accurate representation of the sea-land interface, necessary for simulating swash motions, is obtained. These issues evidently illustrate the robustness of the model. By providing the open source SWASH code (swash.sourceforge.net) that can be freely redistributed and modified, we hope to encourage everyone to further improve the overall performance of the model.

Acknowledgements

Many thanks are due to Jacco Groeneweg and Marcel van Gent from Deltares, the Netherlands for making available experimental data for the Petten Sea defence. The authors are also grateful to Marien Boers (Deltares) for providing his valuable measurements of the laboratory barred surf zone experiments. Our former MSc student Robert Jacobs is especially acknowledged for his major contributions to the calculation of the rip current system. The authors

are indebted to Yoshiki Yamazaki and Kwok Fai Cheung from University of Hawaii at Manoa, USA for providing the Monai Valley laboratory data.

References

[1] Ai, C., Jin, S. and Lv, B., 2010. A new fully non-hydrostatic 3D free surface flow model for water wave motions. Int. J. Numer. Meth. Fluids, doi:10.1002/fld.2317, in press.

[2] Barrett, R., Berry, M., Chan, T.F., Demmel, J., Donato, J., Dongarra, J., Eijkhout, V., Pozo, R., Romine, C. and Van der Vorst, H., 1994. Templates for the solution of linear systems: Building blocks for iterative methods. 2nd edition, SIAM, Philadelphia, PA. Accessible from http://www.netlib.org/templates/Templates.html.

[3] Battjes, J.A. and Janssen, J.P.F.M., 1978. Energy loss and set-up due to breaking of random waves. Proc. 16th Int. Conf. Coastal Engng., ASCE, pp. 569–587.

[4] Becq-Girard, F., Forget, P. and Benoit, M. 1999. Non-linear propagation of unidirectional wave fields over varying topography. Coast. Engng., 38: 91–113.

[5] Beji, S. and Battjes, J.A., 1993. Experimental investigation of wave propagation over a bar. Coast. Engng., 19: 151–162.

[6] Berkhoff, J.C.W., Booij, N. and Radder, A.C., 1982. Verification of numerical wave propagation models for simple harmonic linear water waves. Coast. Engng., 6: 255–279.

[7] Bermudez, A. and Vazquez, M.E., 1994. Upwind methods for hyperbolic conservation laws with source terms. Comput. Fluids, 23: 1049–1071.

[8] Blayo, E. and Debreu, L., 2005. Revisiting open boundary conditions from the point of view of characteristic variables. Ocean Model., 9: 231–252.

[9] Boers, M., 1996. Simulation of a surf zone with a barred beach; Part 1: wave heights and wave breaking. Communication on Hydraulic and Geotechnical Engineering, Report no. 96-5, Delft University of Technology, Delft, The Netherlands.

[10] Booij, N., Ris, R.C. and Holthuijsen, L.H., 1999. A third-generation wave model for coastal regions, 1. Model description and validation. J. Geophys. Res., 104 (C4): 7649–7666.

[11] Briggs, M.J., Synolakis, C.E., Harkins, G.S. and Green, D.R., 1995. Laboratory experiments of tsunami runup on a circular island. Pure Appl. Geophys., 144: 569–593.

[12] Carrier, G.F., Wu, T.T. and Yeh, H., 2003. Tsunami run-up and draw-down on a plane beach. J. Fluid Mech., 475: 79–99.

[13] Casulli, V. and Stelling, G.S., 1998. Numerical simulation of 3D quasi-hydrostatic, free-surface flows. J. Hydr. Eng. ASCE, 124: 678–686.

[14] Chawla A., 1995. Wave transformation over a submerged shoal. M.Sc. thesis, University of Delaware, Newark, USA.

[15] Chen, Q., Dalrymple, R.A., Kirby, J.T., Kennedy, A.B. and Haller, M.C., 1999. Boussinesq modeling of a rip current system. J. Geophys. Res., 104 (C9), 20617-20637.

[16] Cui, H., Pietrzak, J.D. and Stelling, G.S., 2010. A finite volume analogue of the $P_1^{\mathrm{NC}} - P_1$ finite element: with accurate flooding and drying. Ocean Model., 35: 16–30.

[17] Dalrymple, R.A. and Rogers, B.D., 2006. Numerical modeling of water waves with the SPH method. Coast. Engng., 53: 141–147.

[18] Fuhrman, D.R. and Madsen, P.A., 2008. Simulation of nonlinear wave run-up with a high-order Boussinesq model. Coast. Engng., 55: 139–154.

[19] Haas, K.A., Svendsen, I.A., Haller, M.C. and Zhao, Q., 2003. Quasi-three-dimensional modeling of rip current systems. J. Geophys. Res., 108 (C7), doi:10.1029/2002JC001355.

[20] Haller, M.C., Dalrymple, R.A. and Svendsen, I.A., 2002. Experimental study of nearshore dynamics on a barred beach with rip channels. J. Geophys. Res., 107 (C6), doi:10.1029/2001JC000955.

[21] Hansen, W., 1956. Theorie zur Errechnung des Wasserstandes und der Strömingen in Randmeeren nebst Anwendungen. Tellus, 8: 289–300.

[22] Hirt, C.W. and Nichols, B.D., 1981. Volume of fluid (VOF) method for the dynamics of free boundaries. J. Comput. Phys., 39: 201–225.

[23] Holthuijsen, L.H., 2007. Waves in oceanic and coastal waters. Cambridge University Press, Cambridge.

[24] Kramer, S.C. and Stelling, G.S., 2008. A conservative unstructured scheme for rapidly varied flows. Int. J. Numer. Meth. Fluids, 58: 183–212.

[25] Lam, D.C.L. and Simpson R.B., 1976. Centered differencing and the box scheme for diffusion convection problems. J. Comput. Phys., 22: 486-500.

[26] Lynett, P.J., Wu, T.-R. and Liu, P.L.-F., 2002. Modeling wave runup with depth-integrated equations. Coast. Engng., 46: 89–107.

[27] Matsuyama, M. and Tanaka, H., 2001. An experimental study of the highest run-up height in the 1993 Hokkaido Nansei-oki earthquake tsunami. Proc. Int. Tsunami Symposium 2001, Seattle, WA, pp. 879–889.

[28] Ohyama T., Kioka W. and Tada A., 1995. Applicability of numerical models to nonlinear dispersive waves. Coast. Engng., 24: 297–313.

[29] Stansby, P.K. and Zhou, J.G., 1998. Shallow-water flow solver with non-hydrostatic pressure: 2D vertical plane problems. Int. J. Numer. Meth. Fluids, 28: 514–563.

[30] Stelling, G.S., 1983. On the construction of computational methods for shallow water flow problems. Ph.D. thesis, Delft University of Technology, Delft, The Netherlands.

[31] Stelling, G.S. and Duinmeijer, S.P.A., 2003. A staggered conservative scheme for every Froude number in rapidly varied shallow water flows. Int. J. Numer. Meth. Fluids, 43: 1329–1354.

[32] Stelling, G. and Zijlema, M., 2003. An accurate and efficient finite-difference algorithm for non-hydrostatic free-surface flow with application to wave propagation. Int. J. Numer. Meth. Fluids, 43: 1–23.

[33] Stone, H.L., 1968. Iterative solution of implicit approximations of multidimensional partial differential equations. SIAM J. Numer. Anal., 5: 530–558.

[34] Thacker, W.C., 1981. Some exact solutions to the nonlinear shallow-water wave equations. J. Fluid Mech., 107: 499–508.

[35] Van der Vorst, H.A., 1992. Bi-CGSTAB: a fast and smoothly converging variant of Bi-CG for the solution of nonsymmetric linear systems. SIAM J. Sci. Stat. Comput., 13: 631–644.

[36] Van Gent, M.R.A. and Doorn, N., 2000. Numerical model investigations on coastal structures with shallow foreshores; Validation of numerical models based on physical model tests on the Petten Sea-defence. Report H3351, WL|Delft Hydraulics, Delft, The Netherlands.

[37] Van Kan, J.J.I.M., 1986. A second-order accurate pressure correction method for viscous incompressible flow. SIAM J. Sci. Stat. Comput., 7: 870–891.

[38] Van Leer, B., 1979. Towards the ultimate conservative difference scheme. V. A second-order sequel to Godunov's method. J. Comput. Phys., 32: 101–136.

[39] Wei, Y., Mao, X.-Z. and Cheung, K.F., 2006. Well-balanced finite-volume model for long-wave runup. J. Waterw. Port Coast. Ocean Eng., 132: 114–124.

[40] Yamazaki, Y., Kowalik, Z. and Cheung, K.F., 2009. Depth-integrated, non-hydrostatic model for wave breaking and run-up. Int. J. Numer. Meth. Fluids, 61: 473–497.

[41] Yamazaki, Y., Cheung, K.F. and Kowalik, Z., 2011. Depth-integrated, non-hydrostatic model with grid nesting for tsunami generation, propagation, and run-up. Int. J. Numer. Meth. Fluids, doi:10.1002/fld.2485, in press.

[42] Young, C.-C. and Wu, C.H., 2010. A $\sigma-$coordinate non-hydrostatic model with embedded Boussinesq-type like equations for modeling deep-water waves. Int. J. Numer. Meth. Fluids, 63: 1448–1470.

[43] Zhou, J.G. and Stansby, P.K., 1999. 2D shallow water flow model for the hydraulic jump. Int. J. Numer. Meth. Fluids, 29: 375–387.

[44] Zhou, J.G., Causon, D.M., Mingham, C.G. and Ingram, D.M., 2001. The surface gradient method for the treatment of source terms in the shallow-water equations. J. Comput. Phys., 168: 1–25.

[45] Zijlema, M. and Stelling, G.S., 2005. Further experiences with computing non-hydrostatic free-surface flows involving water waves. Int. J. Numer. Meth. Fluids, 48: 169–197.

[46] Zijlema, M. and Stelling, G.S., 2008. Efficient computation of surf zone waves using the nonlinear shallow water equations with non-hydrostatic pressure. Coast. Engng., 55: 780–790.

Table 1

Parallel performance of SWASH for the conical island case with $H = 0.181d$.

p	CPU time (s)	S_p	E_p
1	1489	1.0	1.00
2	585	2.5	1.27
4	332	4.5	1.13
8	171	8.7	1.09
12	123	12.1	1.01
16	95	15.7	0.98
32	63	23.8	0.74

Table 2

Parallel performance of SWASH for the rip current case.

p	CPU time (s)	S_p	E_p
1	25769	1.0	1.00
2	12560	2.1	1.03
4	6371	4.0	1.01
8	3011	8.6	1.07
16	1764	14.6	0.91
32	1194	21.6	0.67

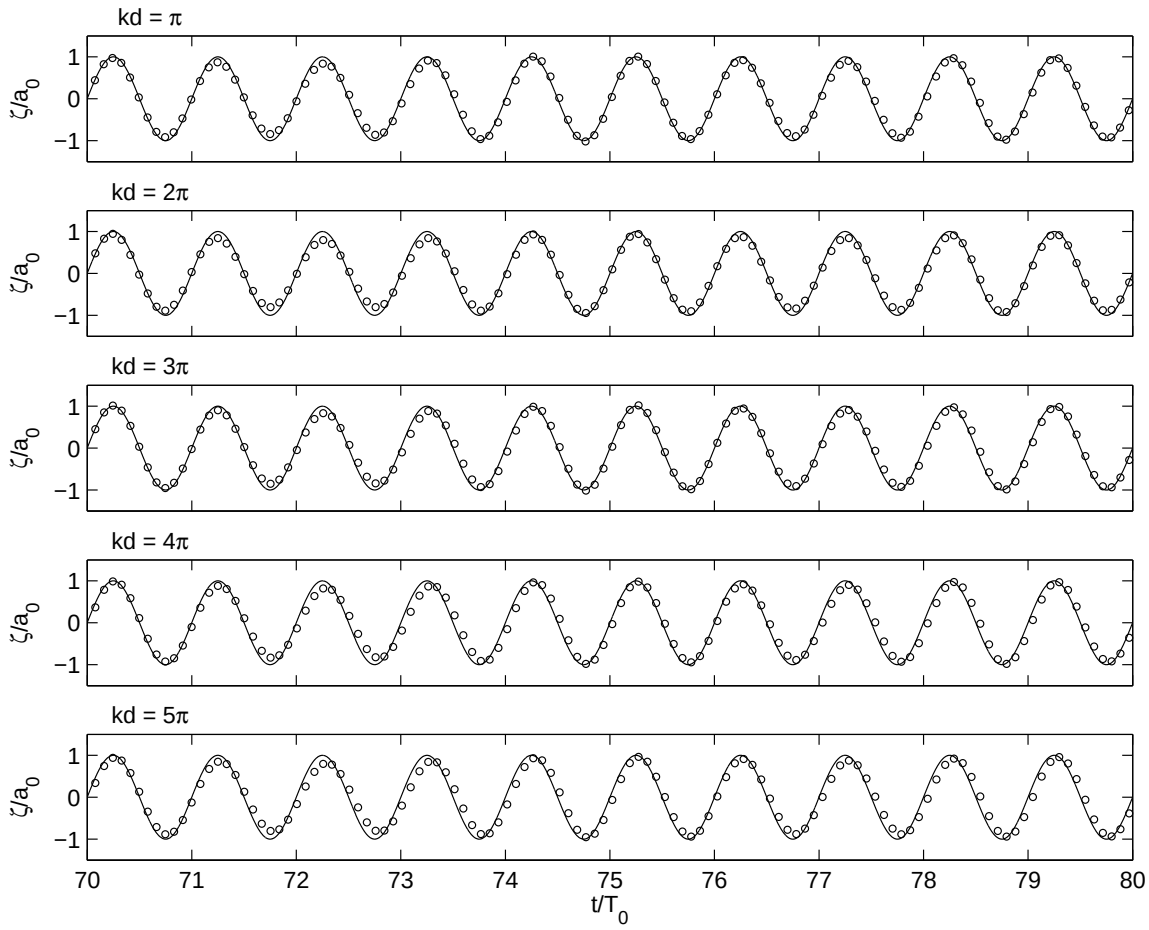

Fig. 1. Computed surface elevations after travelling over a distance of 30 wave lengths obtained with 2 equidistant layers ($kd = \pi$), 3 equidistant layers ($kd = 2\pi$), and 3 layers with thicknesses 10%, 20% and 70% of total depth ($kd = 3\pi$, $kd = 4\pi$, $kd = 5\pi$), compared to the exact ones for linear progressive waves. Exact (solid line), SWASH (circles).

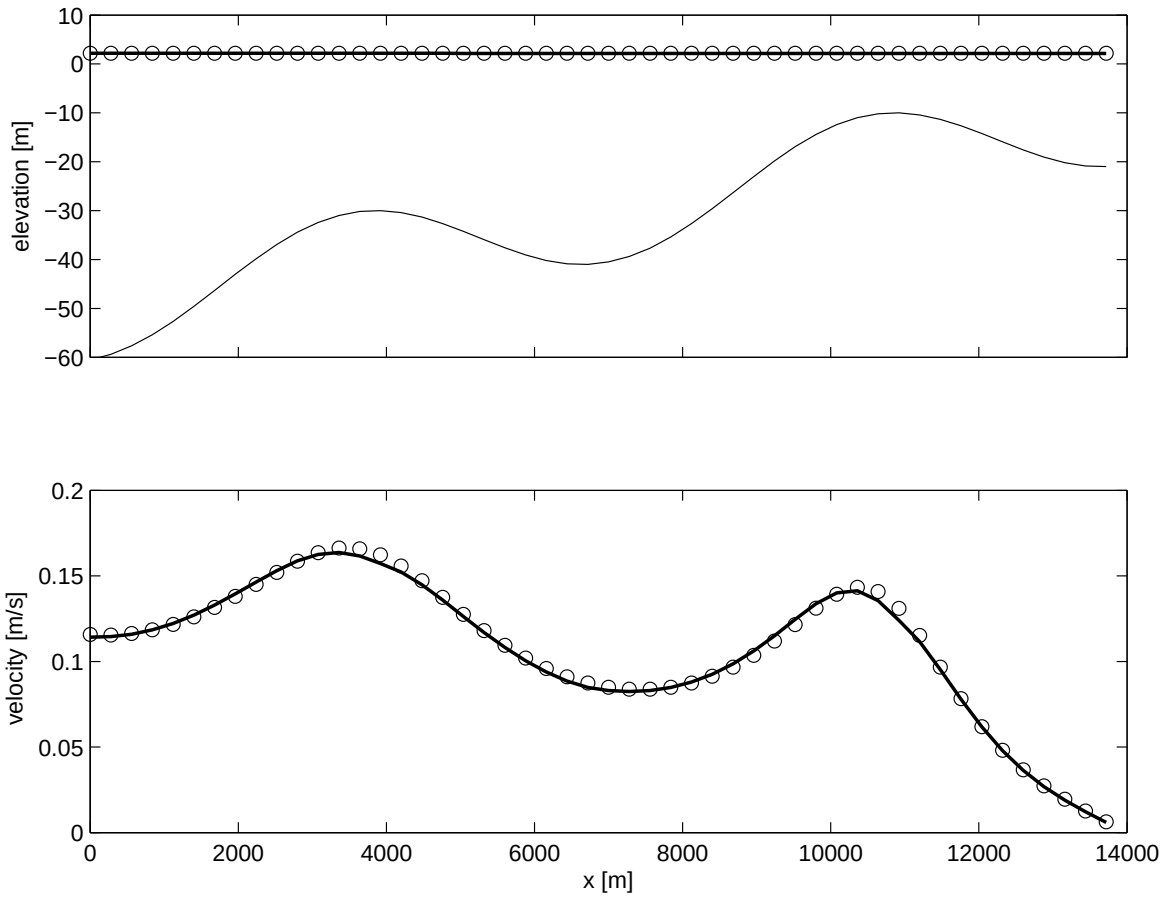

Fig. 2. Predicted water level and flow velocity compared to the analytical ones for the tidal wave over an irregular bottom. Exact (circles), SWASH (thick line), bottom level (thin line).

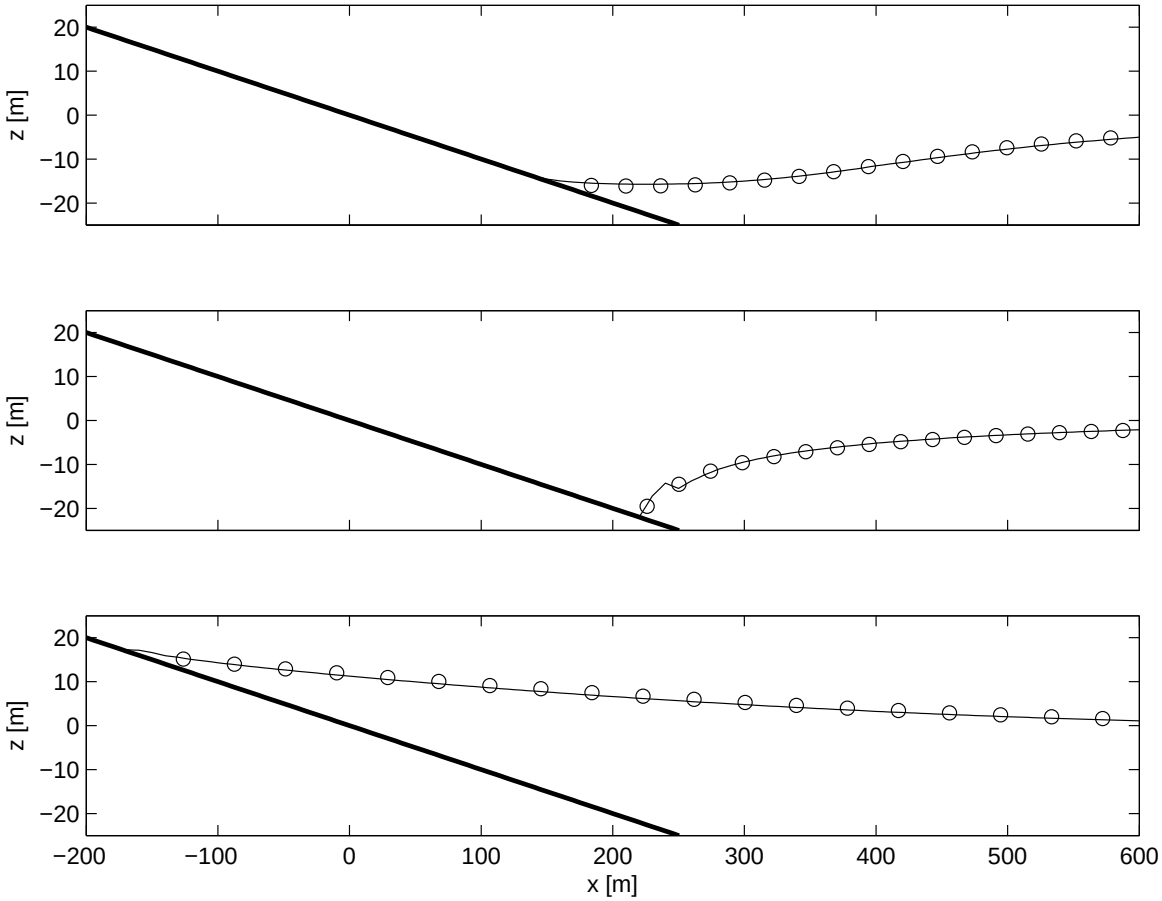

Fig. 3. Comparison of the surface elevation between calculation and analytical solution during tsunami runup at times 160 s (top panel), 175 s (middle panel), and 220 s (bottom panel). Exact (circles), SWASH (thin line).

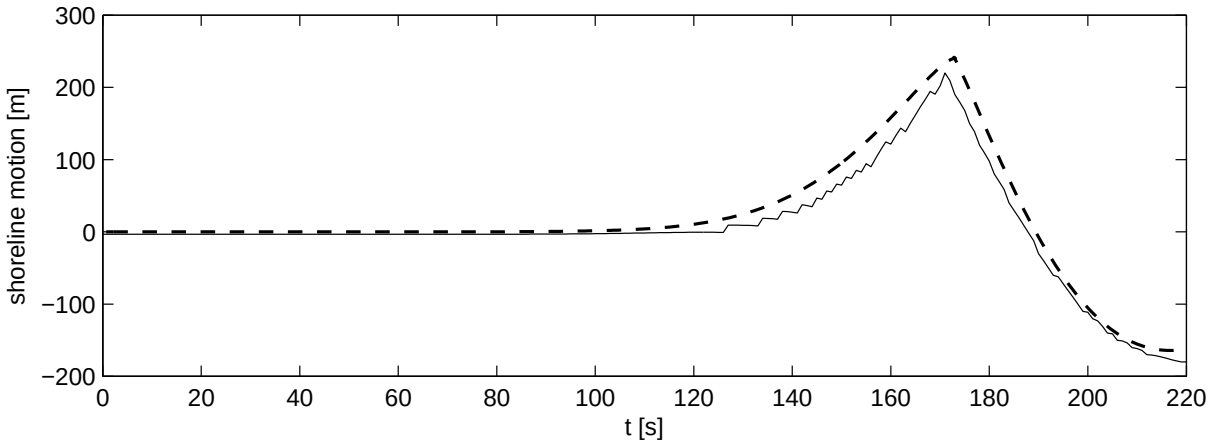

Fig. 4. Computed time series of horizontal shoreline movement compared to the analytical solution for the tsunami runup on a planar beach. Exact (dashed line), SWASH (solid line).

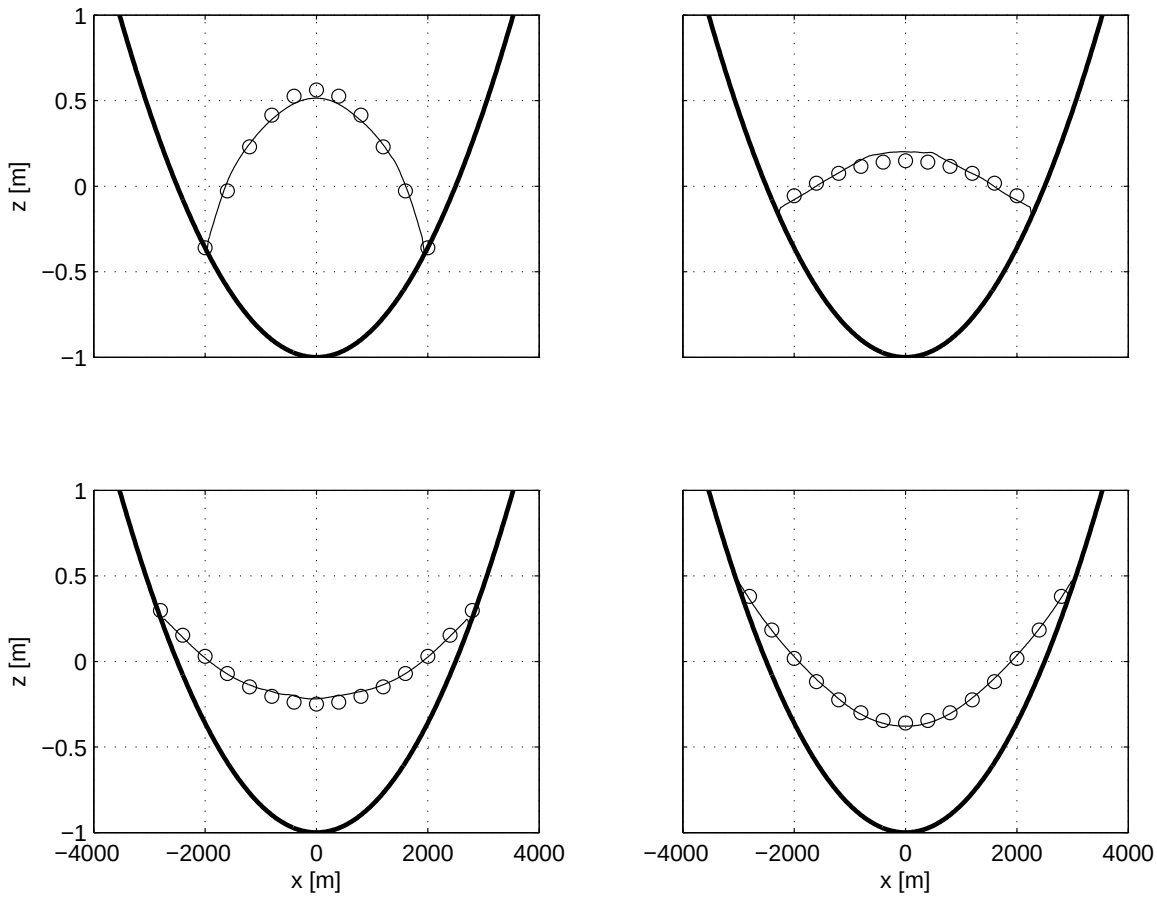

Fig. 5. Computed (thin line) and analytical (circles) centerline free surface profiles for the case of parabolic basin at $t = T$ (top left panel), $t = 7T/6$ (top right panel), $t = 4T/3$ (bottom left panel), and $t = 3T/2$ (bottom right panel).

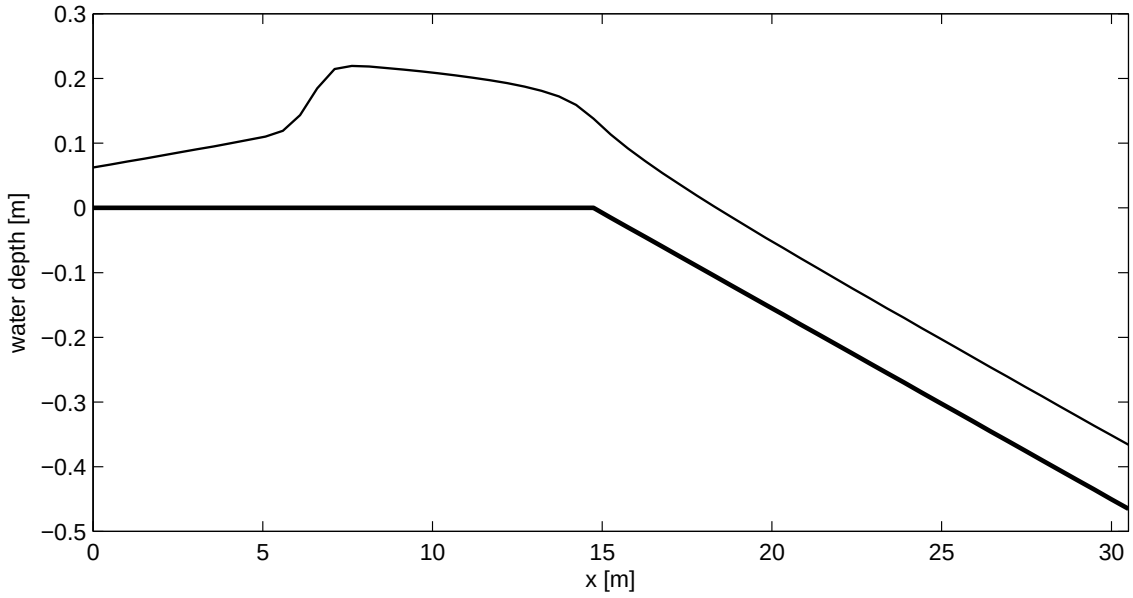

Fig. 6. Steady super- and subcritical flow through a channel with different slopes involving hydraulic jump and drop.

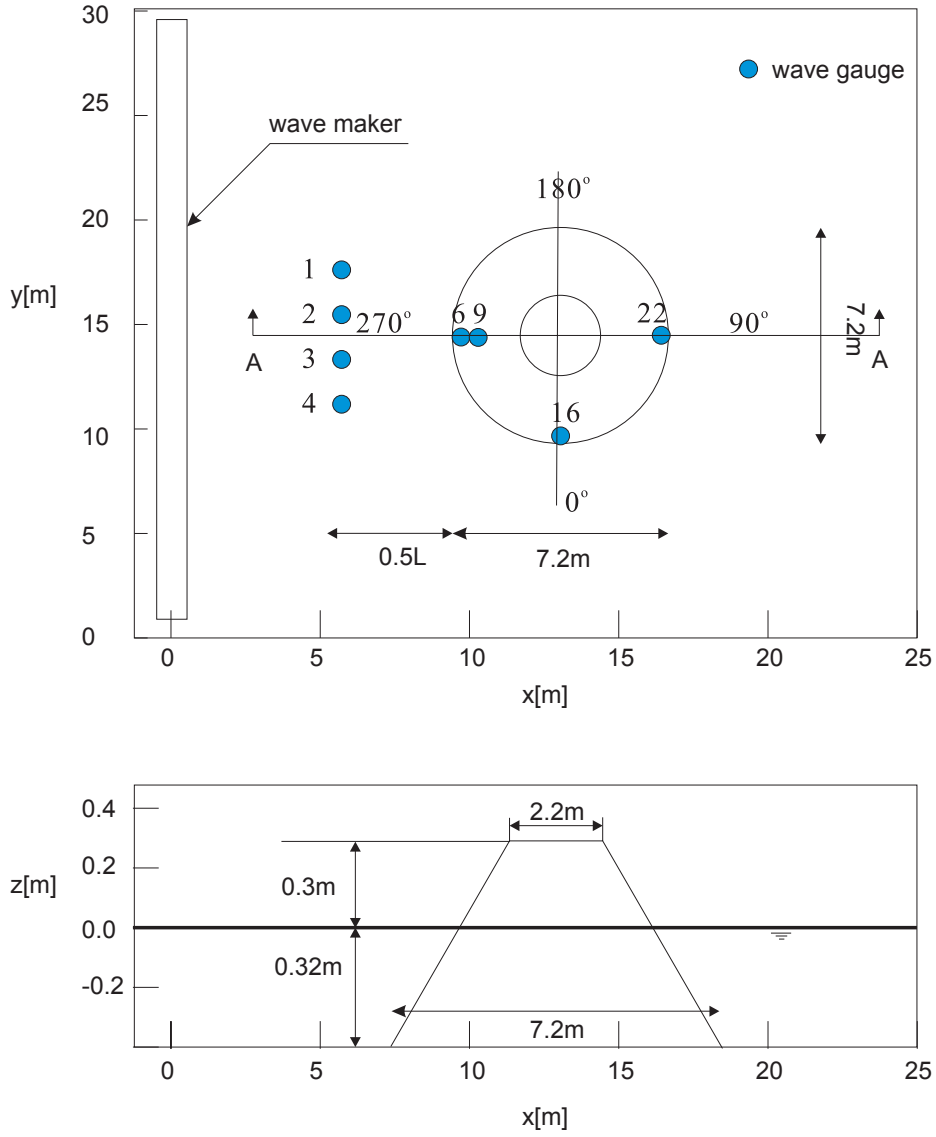

Fig. 7. Schematic views of the conical island experiment. Plane view of the wave basin and the island (top panel) and side view of the island along section A−A (bottom panel). Wave gauges 1 to 4 are located half wave length away from the toe of the island.

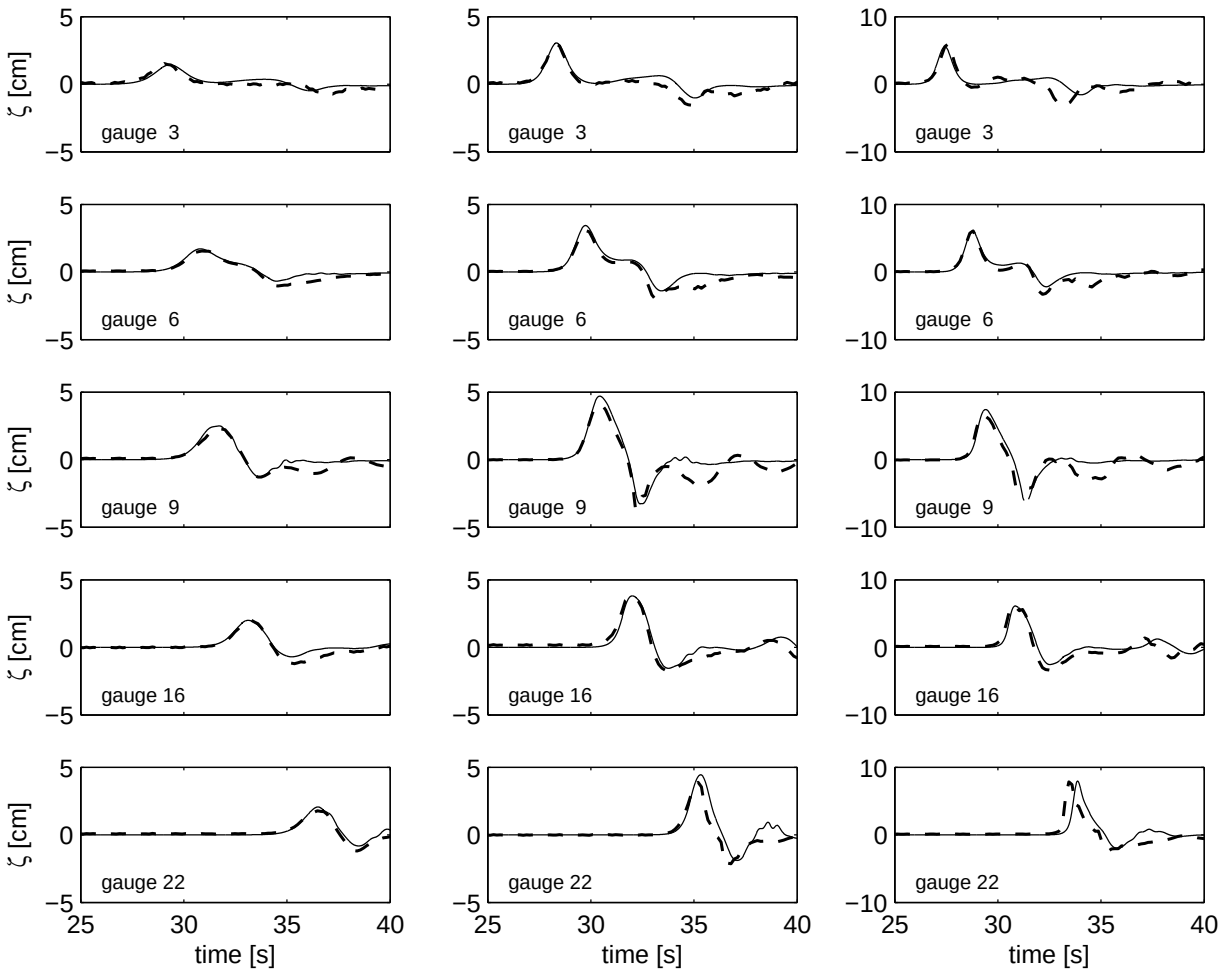

Fig. 8. Comparison with the data of Briggs et al. (1995) for the runup on a conical island: $H = 0.045d$ (left panel), $H = 0.096d$ (middle panel), and $H = 0.181d$ (right panel). Time histories of surface elevation at selected gauges around the island are shown. Dashed line: experimental data; solid line: SWASH.

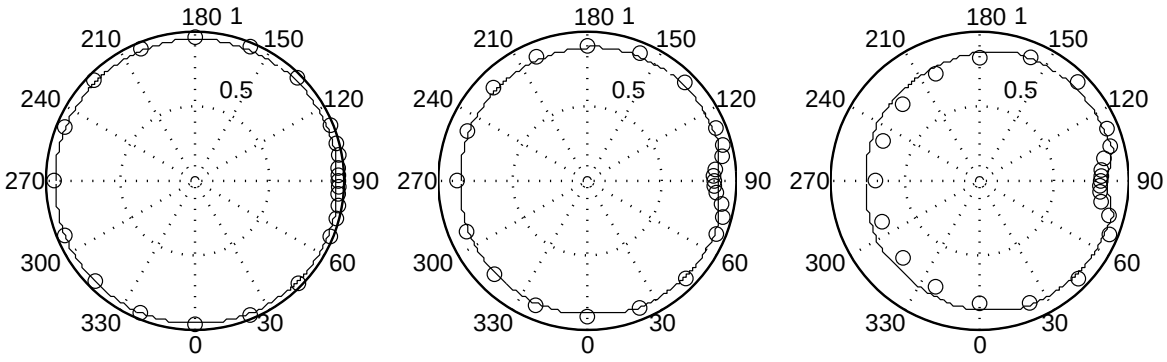

Fig. 9. Computed (solid line) and measured (circles) maximum horizontal runup around the island, relative to the initial shoreline position: $H = 0.045d$ (left panel), $H = 0.096d$ (middle panel), and $H = 0.181d$ (right panel).

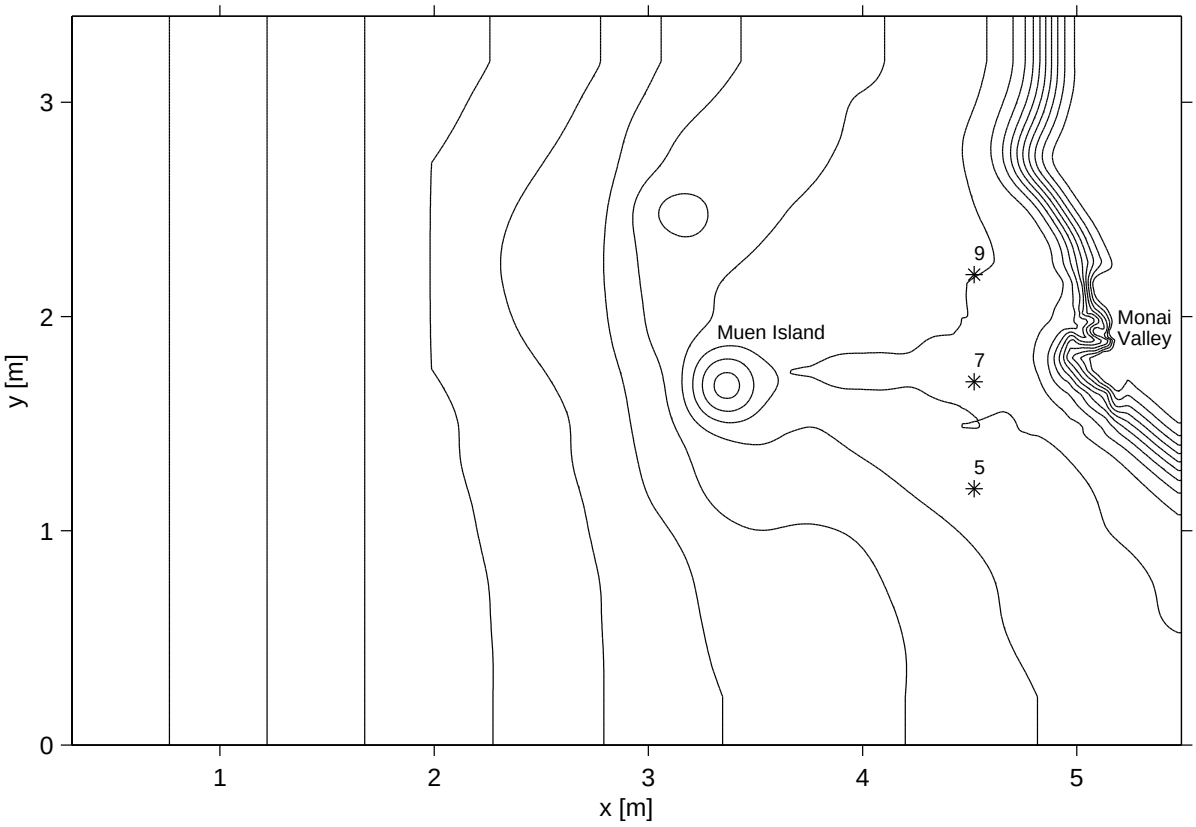

Fig. 10. Bathymetry and computational domain for the Monai Valley runup experiment. Bottom level contours at 0.013-m intervals.

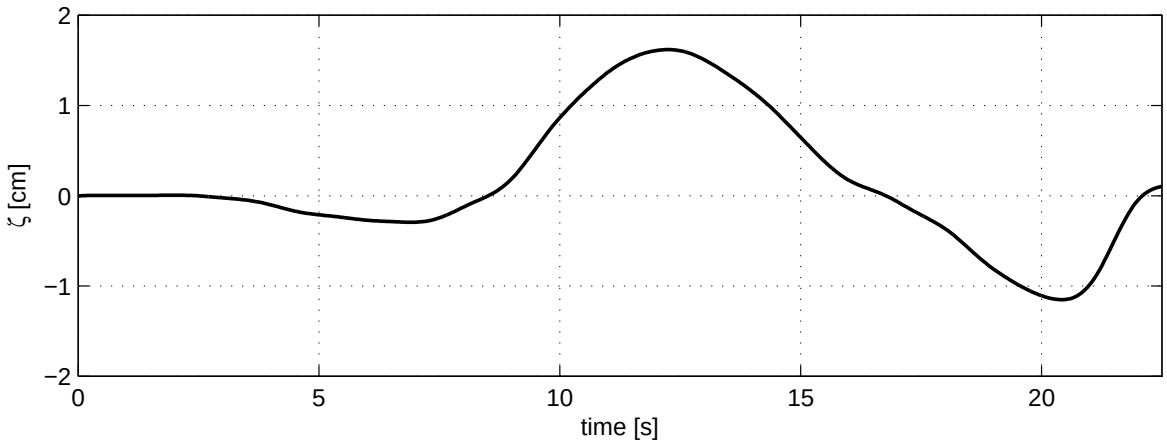

Fig. 11. Input N-wave profile for the Monai Valley runup experiment.

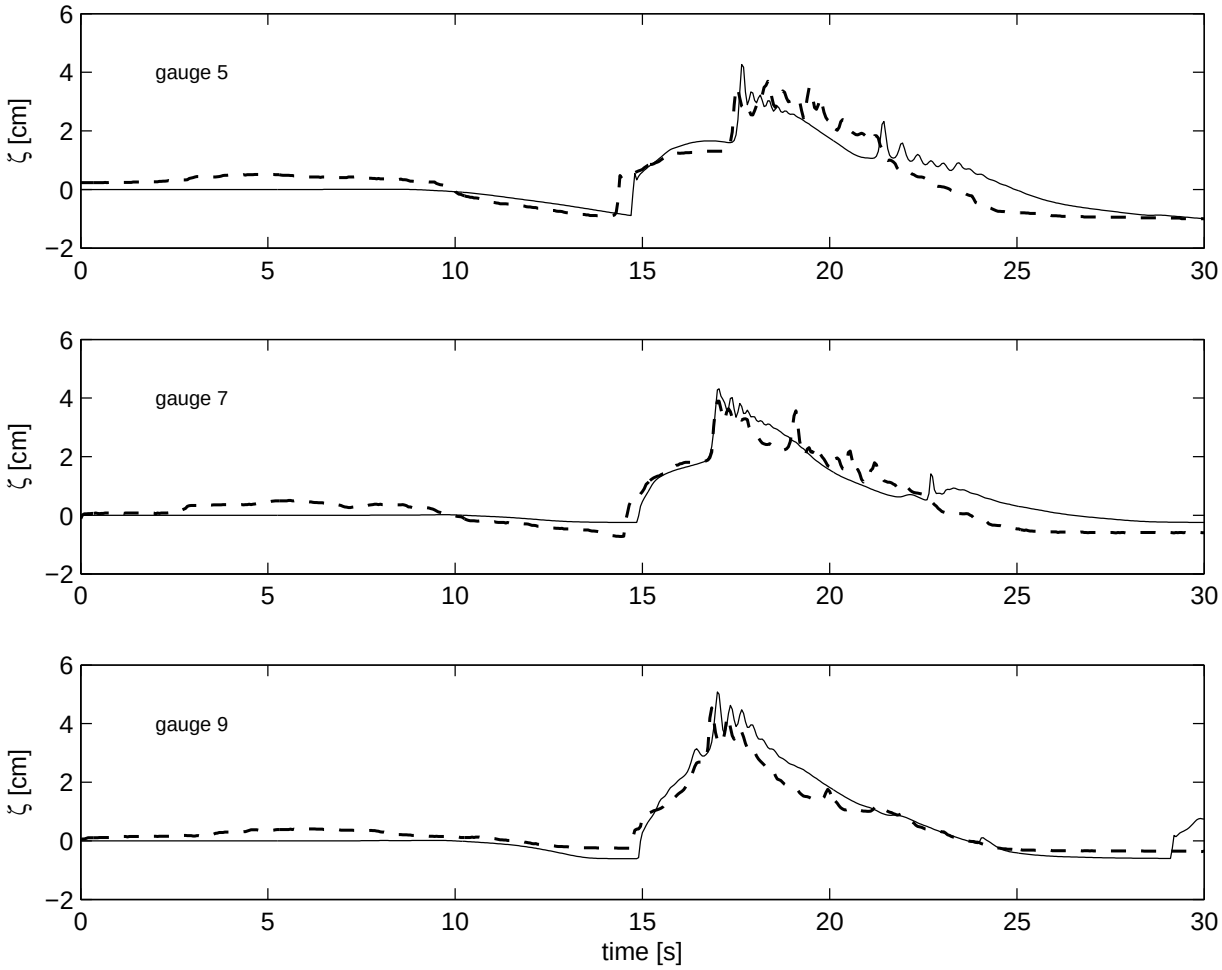

Fig. 12. Comparison of experimental data with numerical simulation results for the Monai Valley runup experiment. Time series of surface elevation at gauges behind Muen Island are shown. Dashed line: experimental data; solid line: SWASH.

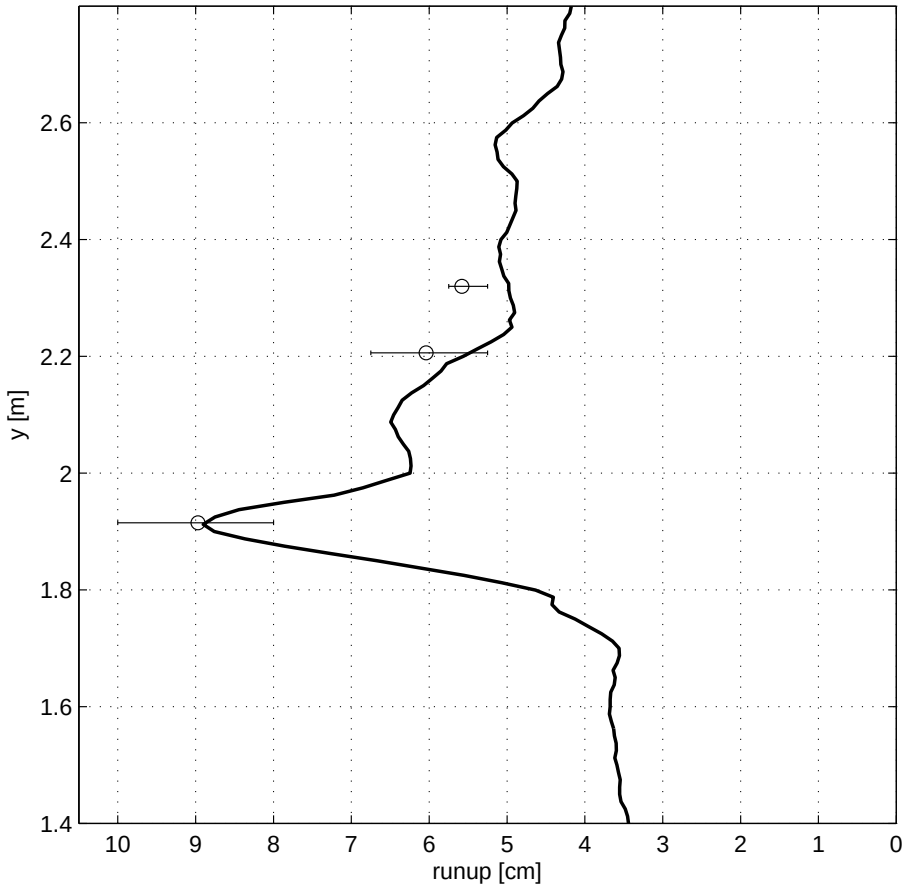

Fig. 13. Comparison of recorded runup with computed runup along the pocket beach with the highest runup height at Monai Valley. Error bars: recorded runup of Matsuyama and Tanaka (2001); solid line: SWASH.

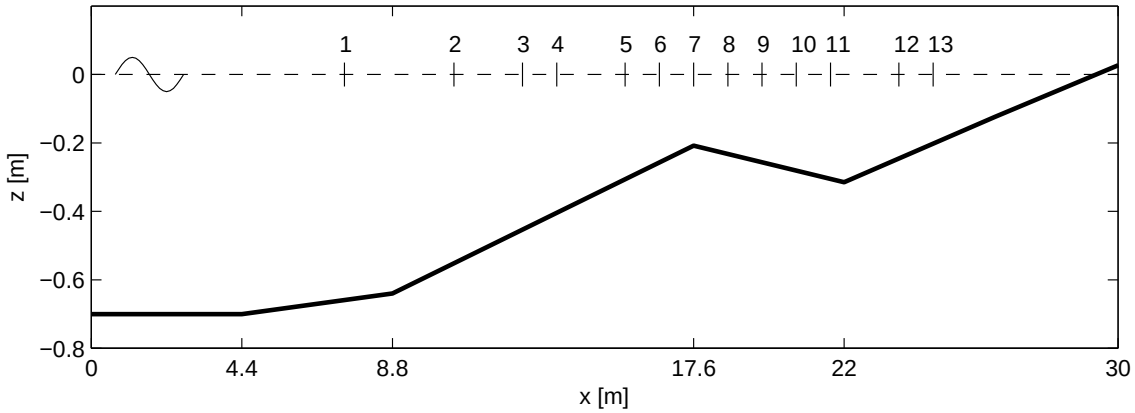

Fig. 14. Sketch of the experimental setup and gauges by Battjes and Janssen (1978).

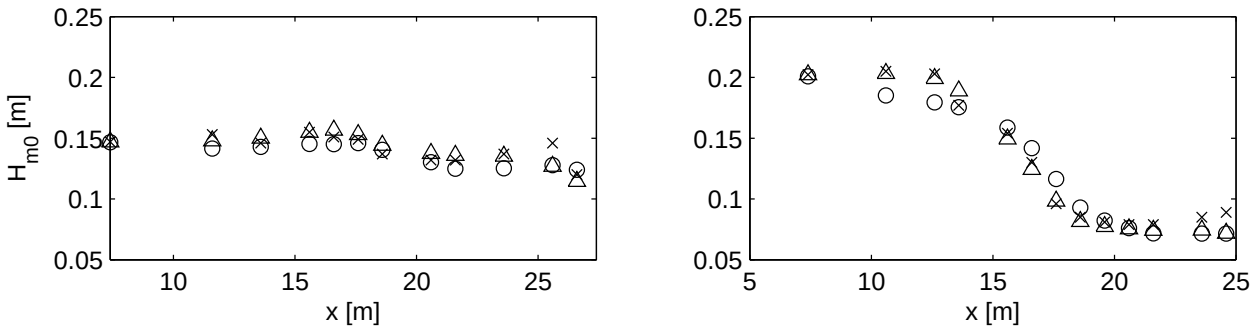

Fig. 15. Computed and measured significant wave heights for the mildly breaking (left panel) and strongly breaking (right panel) cases along the bar-trough beach flume. Crosses: experimental data; circles: SWASH; triangles: SWAN.

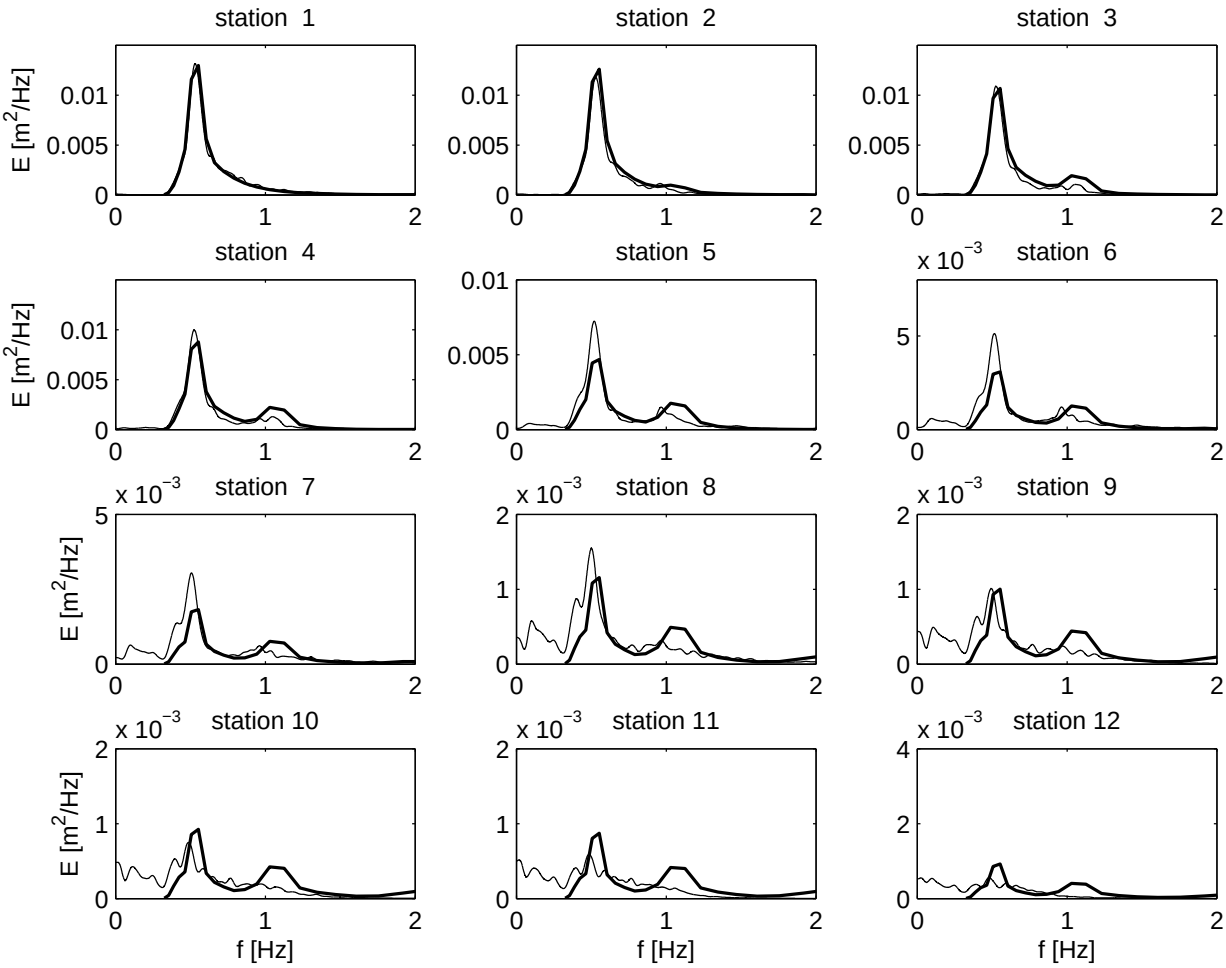

Fig. 16. Comparison of SWASH- and SWAN-computed spatial evolution of energy density spectra for the strongly breaking case of Battjes and Janssen (1978). Thin line: SWASH; thick line: SWAN.

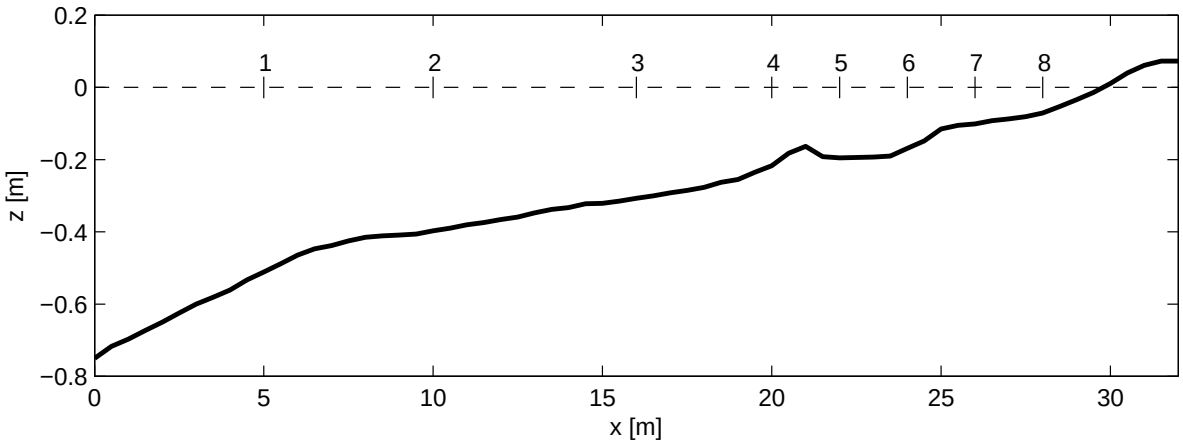

Fig. 17. Bottom topography and location of wave gauges of the experiment of Boers (1996).

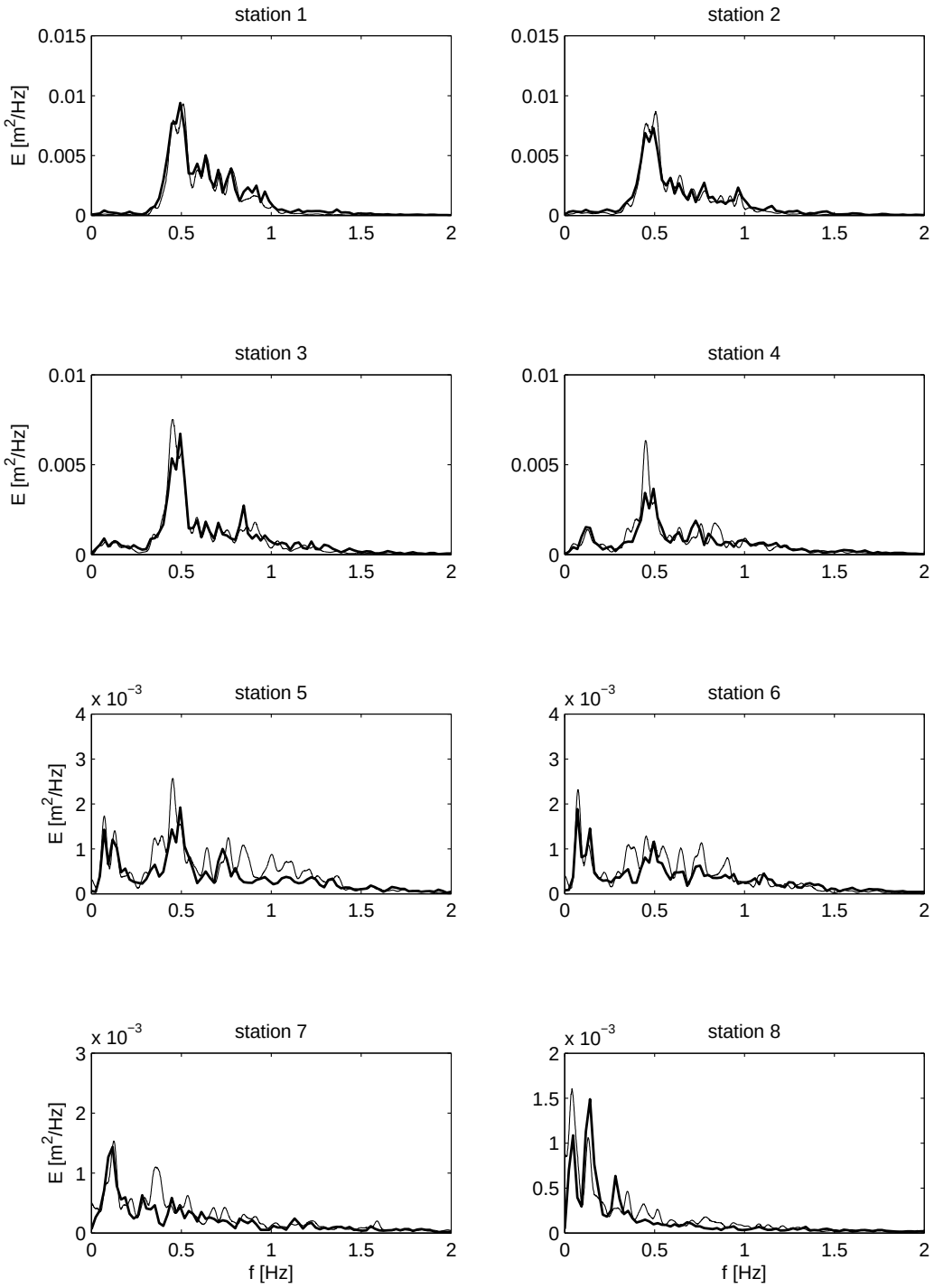

Fig. 18. Observed (thick line) and predicted (thin line) energy density spectra of shoreward propagating waves for case 1B of Boers (1996).

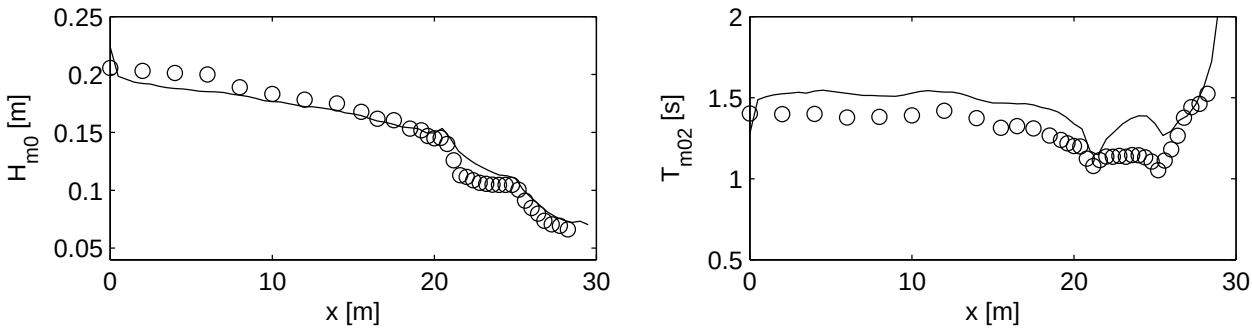

Fig. 19. Computed and measured significant wave heights (left panel) and mean zero-crossing periods (right panel) along the flume for Boers 1B. Circles: experimental data; solid line: SWASH.

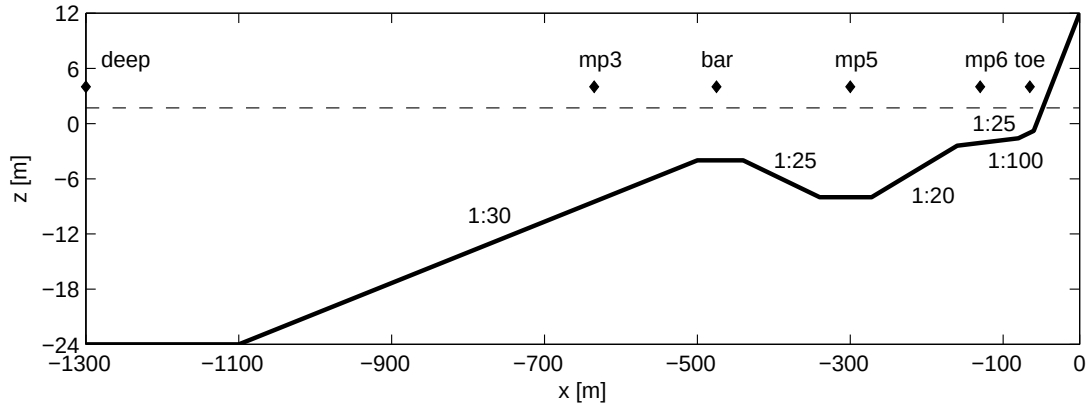

Fig. 20. Lay out of the Petten Sea defence experiment (Van Gent and Doorn, 2000).

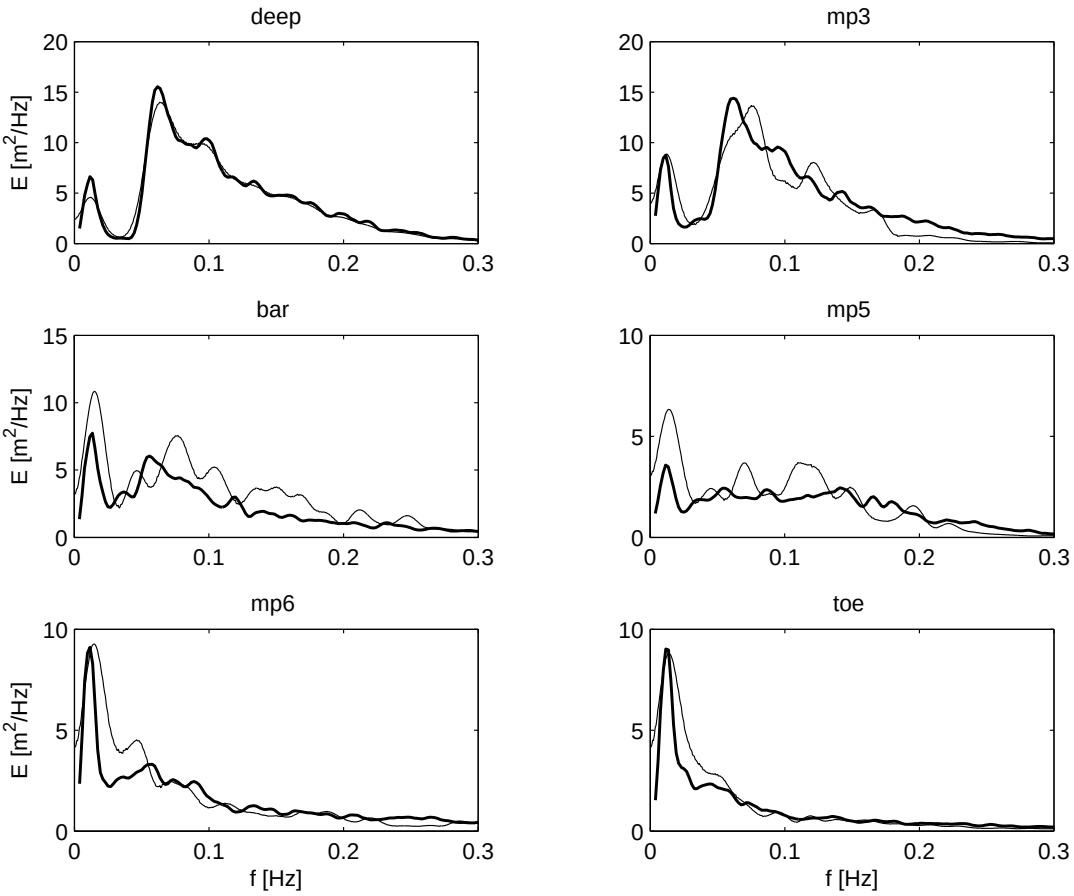

Fig. 21. Computed (thin line) and measured (thick line) energy density spectra at different stations for a storm condition (case 1.04) of the Petten Sea defence experiment.

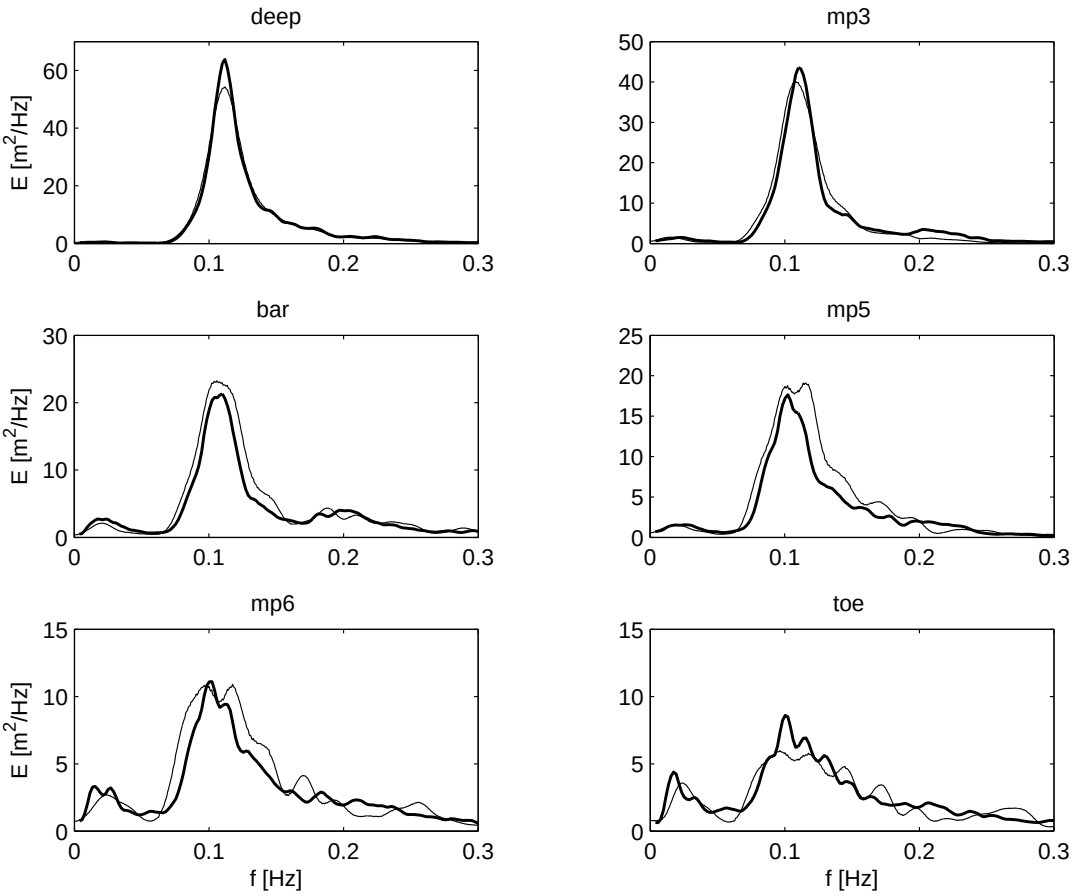

Fig. 22. Computed (thin line) and measured (thick line) energy density spectra at different stations for the case with a relative high steepness (case 2.51) of the Petten Sea defence experiment.

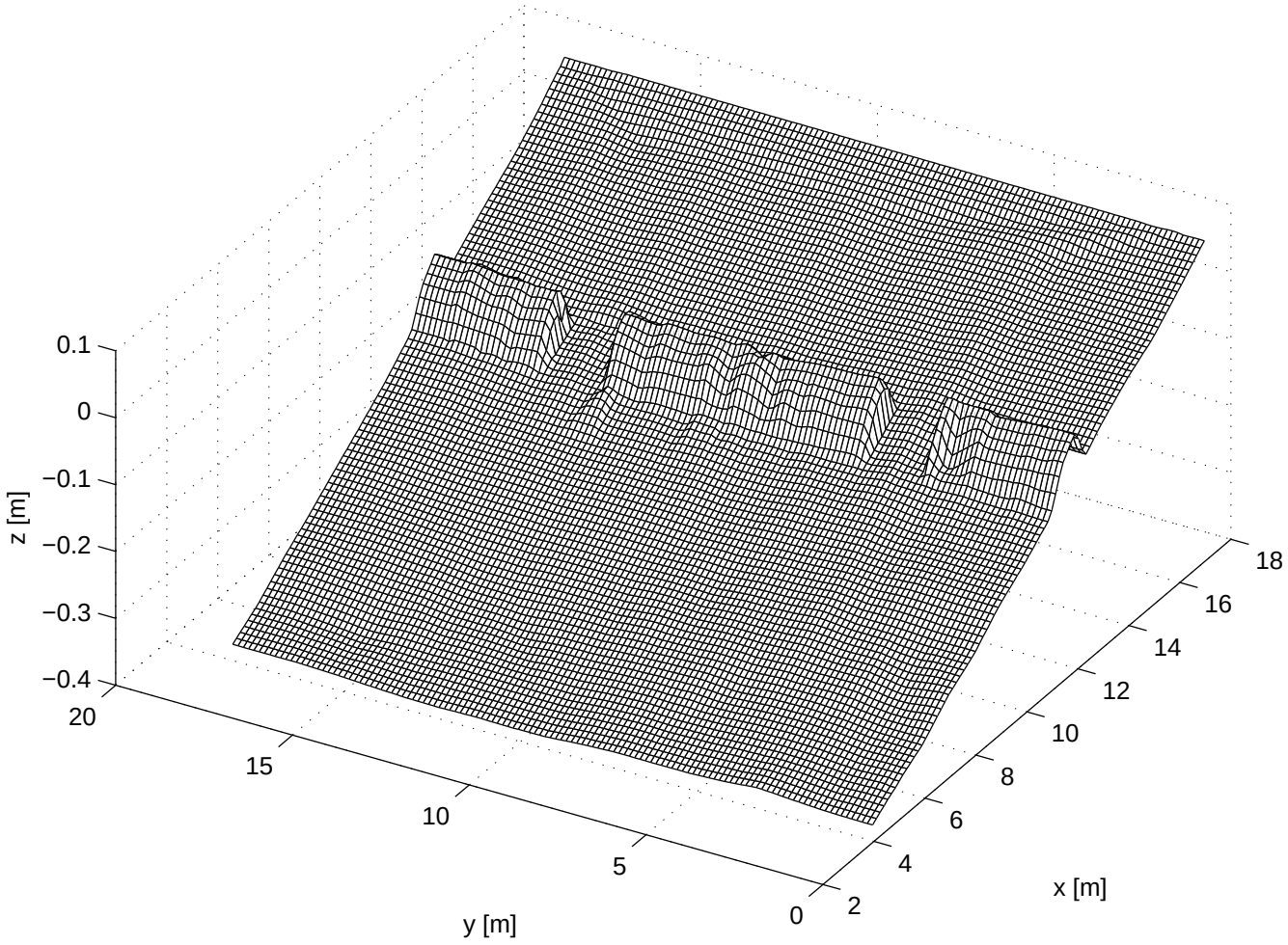

Fig. 23. Bathymetry of a barred beach with rip channels (Haller et al., 2002).

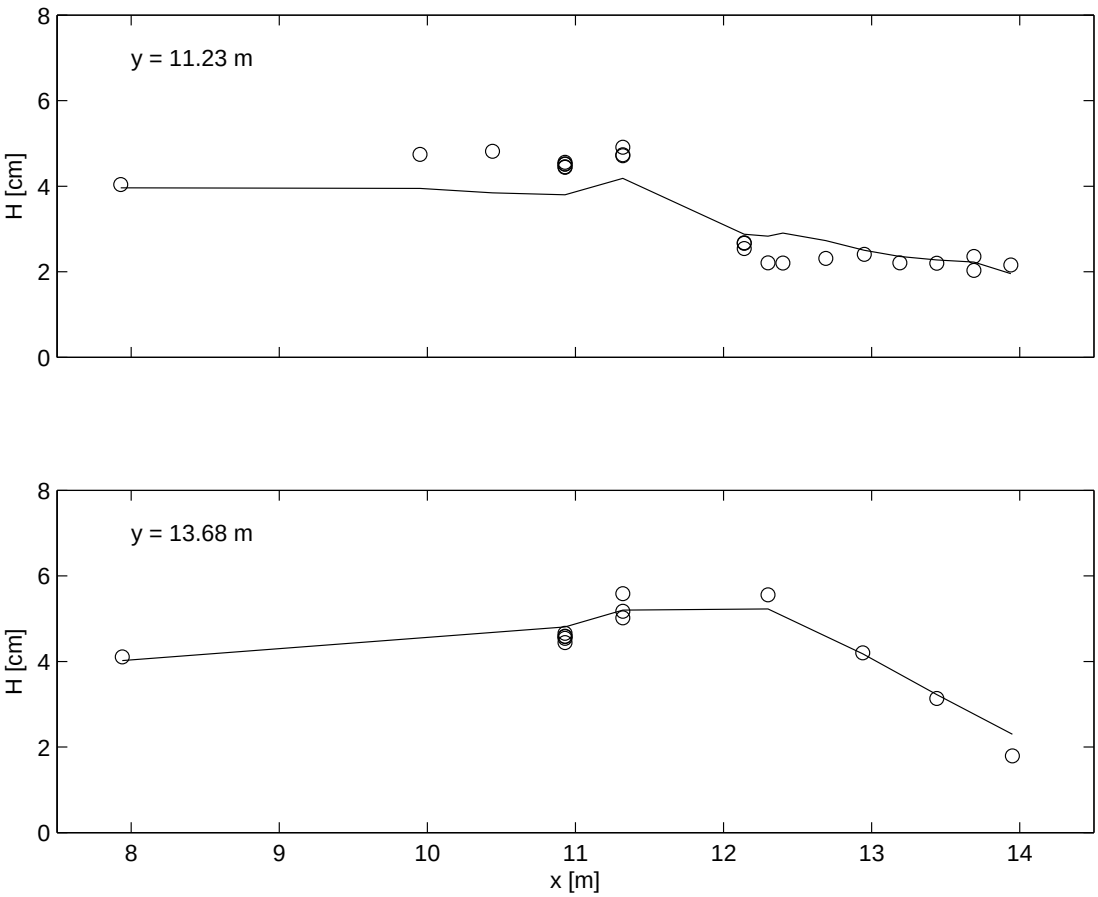

Fig. 24. Comparison between the computed and measured cross-shore variation of the wave height: over the center bar (top panel) and along the center of the rip channel (bottom panel). Circles: experimental data; solid line: SWASH.

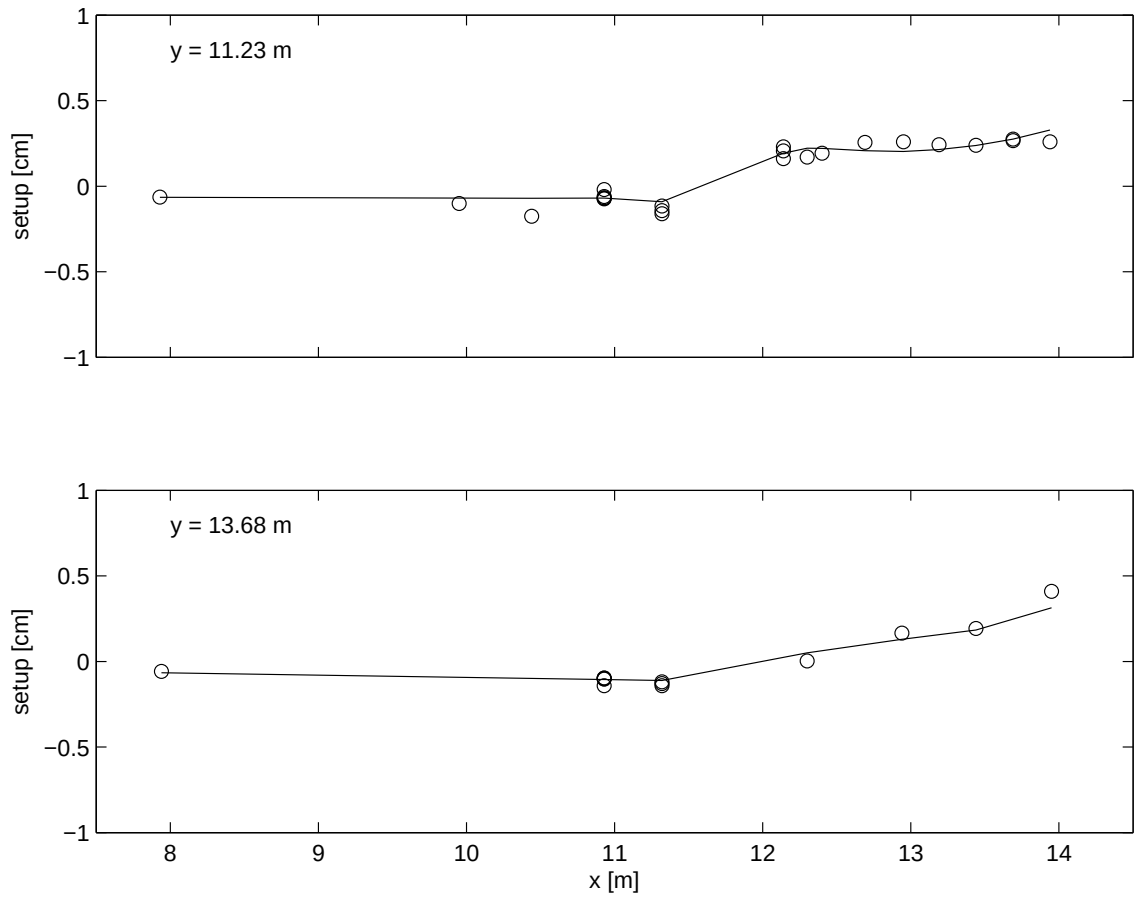

Fig. 25. Comparison between the computed and measured cross-shore variation of the wave-induced setup: over the center bar (top panel) and along the center of the rip channel (bottom panel). Circles: experimental data; solid line: SWASH.

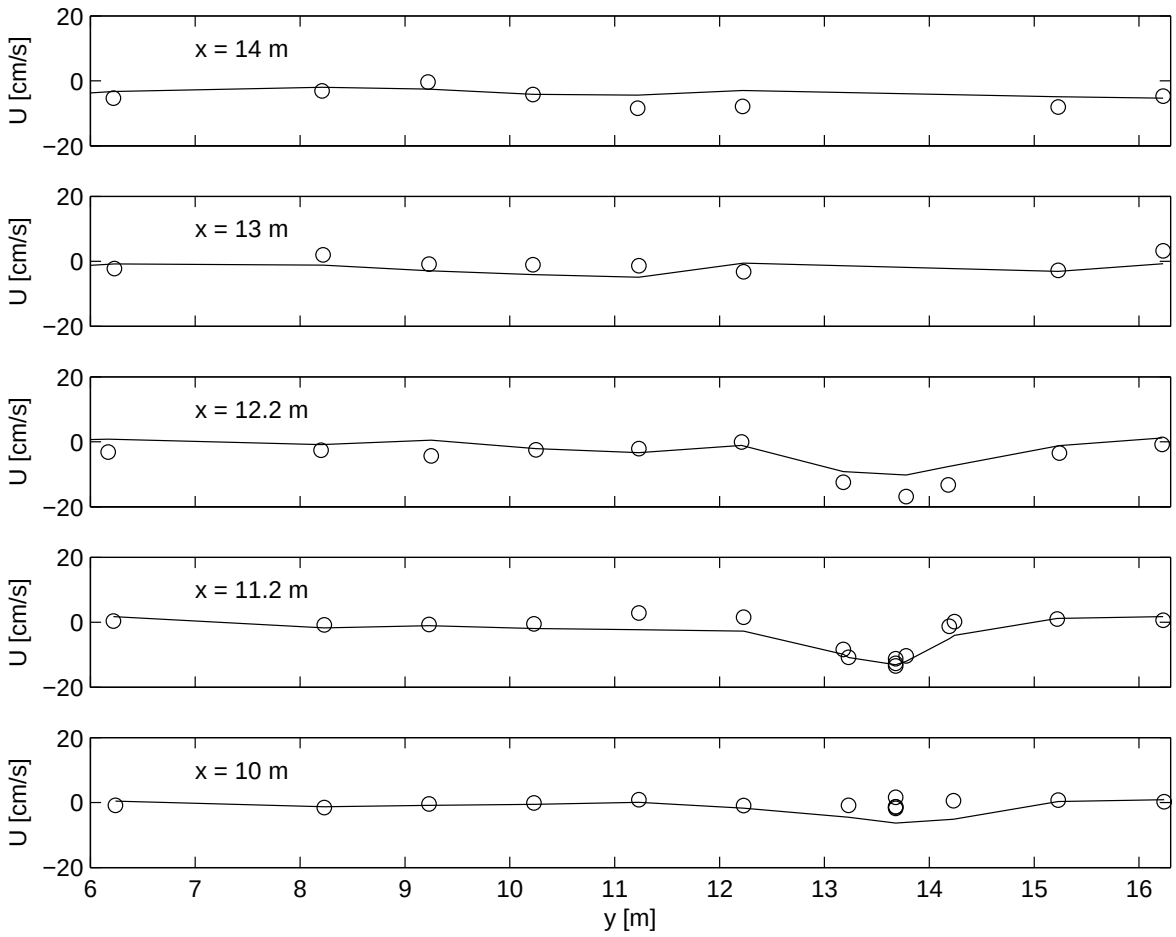

Fig. 26. Longshore variation of the mean cross-shore current at different sections for the rip current case. Circles: experimental data; solid line: SWASH.

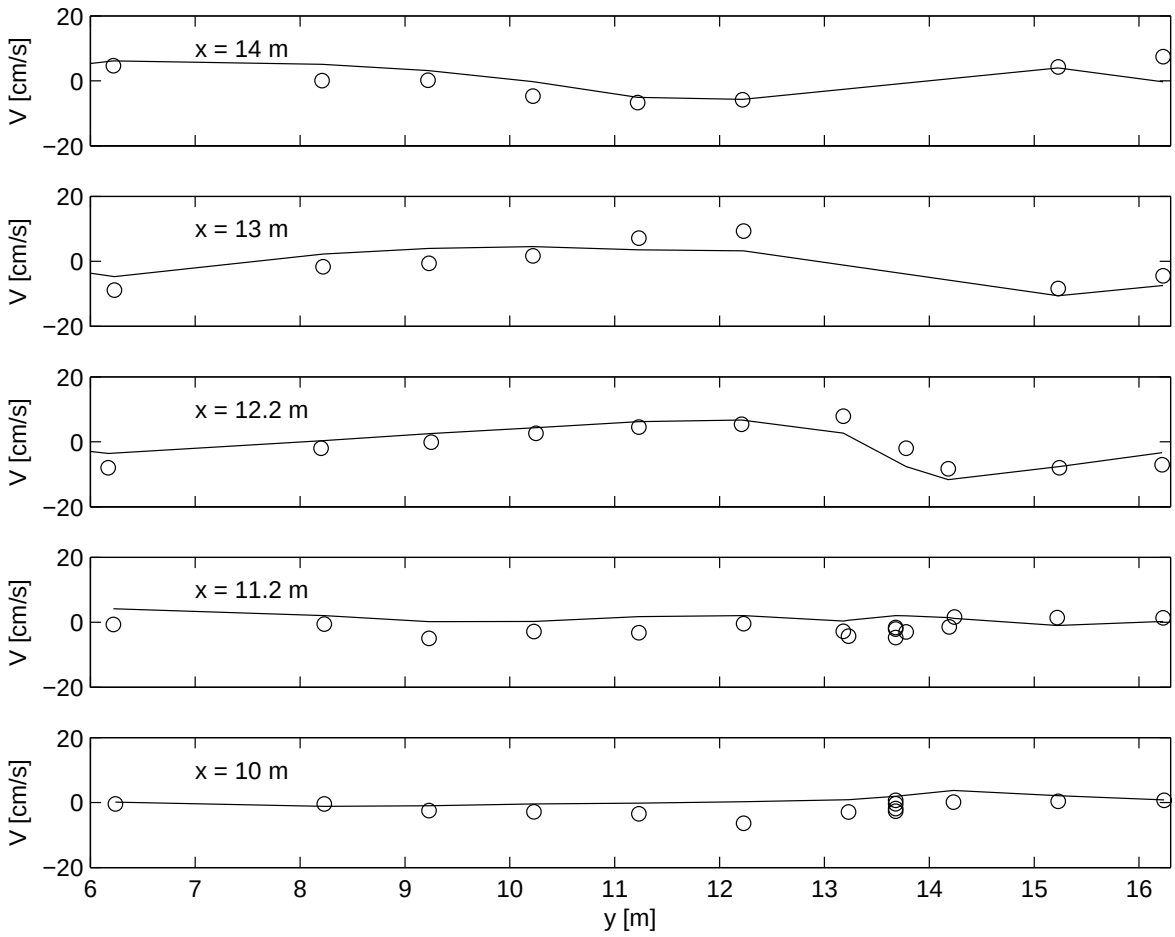

Fig. 27. Longshore variation of the mean longshore current at different sections for the rip current case. Circles: experimental data; solid line: SWASH.